BRNO UNIVERSITY OF TECHNOLOGY
VYSOKÉ UČENÍ TECHNICKÉ V BRNĚ

FACULTY OF MECHANICAL ENGINEERING
FAKULTA STROJNÍHO INŽENÝRSTVÍ

INSTITUTE OF PHYSICAL ENGINEERING
ÚSTAV FYZIKÁLNÍHO INŽENÝRSTVÍ

STUDY OF MAGNONIC CRYSTALS IN A FREQUENCY DOMAIN
STUDIE MAGNONICKÝCH KRYSTALŮ VE FREKVENČNÍ DOMÉNĚ

MASTER'S THESIS
DIPLOMOVÁ PRÁCE

AUTHOR
AUTOR PRÁCE

Bc. Igor Turčan

SUPERVISOR
VEDOUCÍ PRÁCE

Ing. Michal Urbánek, Ph.D.

BRNO 2017

Master's Thesis Assignment

Institute:	Institute of Physical Engineering
Student:	**Bc. Igor Turčan**
Degree program:	Applied Sciences in Engineering
Branch:	Physical Engineering and Nanotechnology
Supervisor:	**Ing. Michal Urbánek, Ph.D.**
Academic year:	2016/17

As provided for by the Act No. 111/98 Coll. on higher education institutions and BUT Study and Examination Regulations, the director of the Institute hereby assigns the following topic of Master's Thesis:

Study of magnonic crystals in a frequency domain

Brief description:

Magnonics is the field of magnetism, which study spin waves (also called magnons). The use of magnons allows the implementation of novel wave-based computing technologies free from the drawbacks inherent to modern electronics, such as dissipation of energy due to Ohmic losses. The research in this area currently focuses on the study of the structures with the active response in frequency domain, so called magnonic crystals. Fabrication and characterization of these structures is essential for application of e.g. magnonic logic circuits. The topic of master's thesis is a fabrication and study of magnonic crystals.
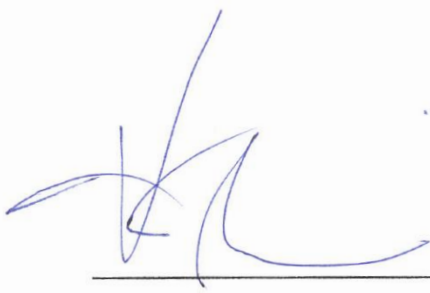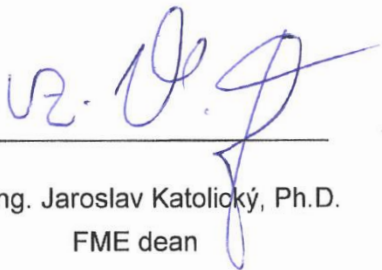
Master's Thesis goals:

Perform a research study of the issues of fabrication and characterization of magnonic crystals.
Design and fabricate magnetic structures with the properties of magnonic crystal.
Design and assemble an instrument for measuring these structures in frequency domain. Study the response of fabricated magnonic crystals.

Bibliography:

NEUSSER, S. et al. Spin waves in antidot lattices: from quantization to magnonic crystals. 2011. PhD Thesis. Technische Universität München.

CHUMAK, A. V. et al. Magnon spintronics. Nature Physics, 2015, 11.6: 453-461.

Students are required to submit the thesis within the deadlines stated in the schedule of the academic year 2016/17.

In Brno, 15. 11. 2016

L. S.

prof. RNDr. Tomáš Šikola, CSc.
Director of the Institute

doc. Ing. Jaroslav Katolický, Ph.D.
FME dean

Abstract

Characterization of magnetodynamic properties of nanomagnets and nanostructured magnetic materials requires methods appropriate for probing the typical timescales of these systems, i.e. in the sub-nanosecond range. The lack of appropriate time-domain characterization techniques is linked to the limits of current electronics. Other possible approach is to use the frequency domain characterization in GHz range. The most common frequency domain characterization technique is the ferromagnetic resonance (FMR) measurement. From FMR spectra it is possible to extract valuable information about the magnetic system: the damping parameter, saturation magnetization etc. The method we utilize for detection of spin-wave excitations aims for the simplification of the characterization experiment. We employ the thermoelectric detection of spin waves in magnetic strips via anomalous Nernst effect. The method is based on the heat generation inside a magnetic film due to the relaxation of spin waves to the lattice. The dissipation of spin-wave energy heats the magnetic strip and creates a temperature gradient towards the substrate (perpendicular to the surface). This leads to generation of an electric field perpendicular to both the temperature gradient and the magnetization direction. The voltage is usually in the µV range, hence it can be measured with common laboratory equipment. Despite its simplicity, this method yields very interesting results and can be used for characterization of magnonic waveguides, magnonic metamaterials, spin-wave emitters and other spin-wave devices.

Abstrakt

Popis magnetodynamických vlastností nanomagnetů a nanostrukturovaných magnetických materiálů vyžaduje metody vhodné pro zkoumání typické časové odezvy těchto systémů, tj. v řádu nanosekund a méně. Nedostatek technik, vhodných právě pro charakterizaci v časové doméně, je spojen s možnostmi současné elektroniky. Další možný přístup, jak popsat vlastnosti nanomagnetů, je charakterizace ve frekvenční doméně v pásmu GHz. Nejrozšířenější technikou charakterizace ve frekvenční doméně je měření feromagnetické rezonance (FMR). Ze spekter FMR lze získat cenné informace o systému: parametr tlumení, saturační magnetizace atd. Metoda, kterou využíváme k detekci excitací spinových vln, má za cíl zjednodušení charakterizace. Využíváme termoelektrickou detekci spinových vln v magnetických drátech prostřednictvím anomálního Nernstova jevu. Metoda je založena na disipaci tepla uvnitř magnetické vrstvy v důsledku útlumu spinových vln, a proto dochází k vytvoření teplotního gradientu směrem k substrátu (kolmo k povrchu). To vede k vytvoření elektrického pole kolmého jak na teplotní gradient, tak na směr magnetizace. Napětí je obvykle v řádu µV, proto může být měřeno obvyklým laboratorním vybavením. Navzdory své jednoduchosti poskytuje tato metoda velmi zajímavé výsledky a může být použita pro charakterizaci magnonických vlnovodů, magnonických metamateriálů, emitorů spinových vln a dalších zařízení, pracujících se spinovými vlnami.

Keywords
magnonics, anomalous Nernst effect, ferromagnetic resonance, excitation and detection of spin waves.

Klíčová slova
magnonika, anomální Nernstův jev, feromagnetická rezonance, excitace a detekce spinových vln.

TURČAN, Igor. *Study of magnonic crystals in a frequency domain.* Brno, 2017. 53 p. Master's thesis. Brno University of Technology. Faculty of Mechanical Engineering. Supervised by Michal URBÁNEK.

I hereby declare that I have written my master's thesis on the theme of *Study of magnonic crystals in a frequency domain* independently, under the guidance of the master's thesis supervisor, Ing. Michal Urbánek, Ph.D., and using the technical literature and other sources of information which are all properly quoted in the thesis and detailed in the list of literature at the end of the thesis.

....

                Place and date   Bc. Igor Turčan

Acknowledgment

I would like to express my sincere gratitude to my supervisor Dr. Michal Urbánek for his guidance and inspiring comments. I have benefited greatly from his knowledge and opportunities he has given me. On the equal foot, I am deeply indebted to Lukáš Flajšman for teaching me the concepts of magnonics, his brilliant ideas, leadership and neverending support when dealing with many difficulties. It was an honour to work with him. I am very greateful to Marek Vaňatka for his invaluable help with the experimental part of the thesis. I would like to thank Vojtěch Švarc who taught me the art of cleaning. I also owe gratitude to my friends and colleagues in the magnetism group at the Institute of Physical Engineering. It was a great and enriching experience to work there on a daily basis. I wish to thank Prof. Jiří Spousta for a critical reading of my thesis and his valuable suggestions and comments. Above all, I would like to thank my girlfriend Míša for the mental support, endless patience, love and understanding. Finally, I am thankful to my parents for their support during my whole life. Although you will probably not read this thesis, for everything I have ever achieved in my life, I owe you.

Děkuji.

<div align="right">Bc. Igor Turčan</div>

Contents

1. Introduction

The incredible progress in information technology, the so called digital revolution, has significantly changed life in the last decade. In the field of spintronics, the electron's spin rather than the electron's charge is used. The field has the potential to replace common semiconductor electronics [1, 2]. One of the biggest achievements in this field was the discovery of the giant magnetoresistance (GMR) effect in 1988 by A. Fert and P. Grünberg [3, 4] or the so-called spin transfer torque (STT) effect in 1996 by L. Berger and J. C. Slonczewski [5, 6].

Another route for information transfer and processing is provided in the emerging field of magnonics, where the processing is done via spin waves [7–9]. Spin waves are collective oscillations of magnetic moments in magnetically ordered materials and their quanta are called magnons. Magnons might be potential information carrier, due to their capability of transferring an information without moving electric charge.

The particular role in magnonics is played by periodically altered structures, so called magnonic crystals [10]. The periodic alteration might be done using different magnetic materials, different shapes, or local variation of the bias field. In magnonic crystals, an artificially tailored band structure is formed. The band spectrum consists of allowed minibands and forbidden frequency gaps, where there are no allowed magnonic states. Magnonic crystals are, due to these properties, suitable candidates for applications, e.g. microwave filters, switchers, power limiters, etc.

Spin caloritronics [11, 12], another sub-field of spintronics, has attracted interest in research community recently. Spin caloritronics focuses on the interaction between spin, charge, and heat currents. Although thermoelectric and thermomagnetic effects are known since 1830's, thermomagnetic effects recently get much attention due to discoveries of new fascinating phenomena.

In this thesis, such a novel approach is devised and applied for detection of spin waves. The response of the magnonic crystal is measured thermoelectrically via anomalous Nernst effect (ANE) [13]. Due to the relaxation of spin waves to the lattice, the electric field is generated in the ferromagnetic material. The generated voltage is described by the ANE.

The thesis is organized as follows:

Chapter 2 explains the relevant theoretical background, which is needed to understand the experimental part of the thesis. A brief introduction to ferromagnetism together with the most important magnetic interactions is given. Subsequently, a fundamental description of the magnetization dynamics and the Landau-Lifshitz-Gilbert equation are provided. Afterwards, concept of spin waves is introduced and their dispersion relations are presented. Magnonic crystals and magnonic devices are described next. In the last part of the chapter, the thermoelectric essentials are discussed.

In Chapter 3, the experimental methods and instruments are described. The principle of electron beam lithography is given. The lift-of method is presented next. Chapter ends with the description of the experimental setup and discussion about coplanar waveguides.

1. INTRODUCTION

Chapter 4 is devoted to the preparation of the samples. In the first part, the sample design is presented. It follows with the process of preparation of samples. Afterwards, the design and preparation of magnonic crystal are discussed. Chapter ends with a section dealing with the problems during fabrication.

Experimental results are presented in detail in Chapter 5. Furthermore, the analysis of the experiment data is provided.

Finally, Chapter 6 summarizes the accomplished experimental results. Ideas and suggestions for the future work are presented.

2. Basic theory of magnetization dynamics

In this chapter, a brief introduction to ferromagnetism and magnonics is provided. It is essential to cover the theoretical background to be able to explain the experimental part of the thesis. The reviews on magnetism [14–17] and on physics of spin waves [18, 19] are followed.

2.1. Ferromagnetism

Ferromagnetism is a characteristic property of materials, that exhibit a spontaneous magnetization $\boldsymbol{M}$ even with no applied external magnetic field $\boldsymbol{H}$. The magnetization $\boldsymbol{M}$ is defined as a magnetic moment $\boldsymbol{\mu}$ of a sample per volume V. The relation between $\boldsymbol{M}$ and $\boldsymbol{H}$ is

$$\boldsymbol{M} = \hat{\chi} \cdot \boldsymbol{H}, \tag{2.1}$$

where $\hat{\chi}$ is the complex valued susceptibility tensor which describes an anisotropic magnetic response of $\boldsymbol{M}$ on a field $\boldsymbol{H}$. Generally, $\boldsymbol{M}$, $\hat{\chi}$ and $\boldsymbol{H}$ are spatially and time dependent. However, in the isotropic case, where neither $\boldsymbol{H}$ nor $\boldsymbol{M}$ are spatially varying or time dependent, tensor $\hat{\chi}$ is replaced with scalar susceptibility χ.

For description of problems in magnetism, typically so called magnetic flux density $\boldsymbol{B}$ is introduced. The magnetic flux density $\boldsymbol{B}$ is given by

$$\boldsymbol{B} = \mu_0(\boldsymbol{M} + \boldsymbol{H}) = \mu_0 \left(\hat{\chi} + \hat{1} \right) \cdot \boldsymbol{H}, \tag{2.2}$$

where μ_0 is the permeability of vacuum, $\mu_0 = 4\pi \cdot 10^{-7}\,\mathrm{H/m}$, and

$$\hat{\mu} = \hat{\chi} + \hat{1}, \tag{2.3}$$

is the permeability of the material.

2.2. Magnetization and total energy

The quantum mechanical approach is essential for the rigorous treatment of ferromagnetism. The Hamiltonian $\mathcal{H}$, yielding the energy eigenstates of a magnetic spin system reflects the idea of the van Vleck model [20], is written:

$$\mathcal{H} = -2 \cdot \sum_{i>j} J_{ij} \boldsymbol{S}_i \cdot \boldsymbol{S}_j + g\mu_B \sum_i \boldsymbol{S}_i \cdot \boldsymbol{B} + \sum_{i>j} D_{ij} \left[\boldsymbol{S}_j \cdot \boldsymbol{S}_i - 3r_{ij}^{-2} \left(\boldsymbol{r}_{ij} \cdot \boldsymbol{S}_j \right) \left(\boldsymbol{r}_{ij} \cdot \boldsymbol{S}_i \right) \right], \tag{2.4}$$

where J_{ij} is a measure for the strength of the exchange interaction between spins, $\boldsymbol{S}_i$ is the spin moment vector of atom i, g is the Landé factor, μ_B is the Bohr magneton $\mu_B = = \frac{e\hbar}{2m_e}$, D_{ij} is the parameterized dipole-dipole interaction strength and $\boldsymbol{r}_{ij}$ is the vector between spin i and spin j. The first right-hand term of (2.4) is the exchange interaction. The second term corresponds to the Zeeman energy, i.e. interaction of the spins with the external field. The third member embodies the dipole-dipole interaction of the spins.

The Hamiltonian in (2.4) can be generalized for a continuum approach [21]. Then, the major energy contributions are Zeeman, exchange, demagnetizing field and anisotropy energy described in more detail in following sections.

2.2.1. Zeeman energy

The Zeeman energy is at play when the external magnetic field $\boldsymbol{H}_{\text{ext}}$ is present and describes an interaction of the magnetization $\boldsymbol{M}$ with the external magnetic field $\boldsymbol{H}_{\text{ext}}$. The energy density is given by

$$\epsilon_{\text{Z}} = -\frac{\mu_0}{V} \iiint_\Omega \boldsymbol{M} \cdot \boldsymbol{H}_{\text{ext}} \mathrm{d}V \, . \tag{2.5}$$

The minus sign indicates the minimum energy for the magnetization having parallel orientation with the external field.

2.2.2. Exchange energy

Exchange interaction was first introduced by Heisenberg in 1928 [22] in order to explain ferromagnetic ordering at the room temperature, therefore it is responsible for the spontaneous magnetization. It is a direct consequence of Coulomb interaction and Pauli's exclusion law. Two electrons of the same quantum number cannot occupy the same quantum mechanical state. If the spins of these two electrons are antiparallel to each other, the electrons will share a common orbit, thus increasing the electrostatic Coulomb energy. If, however, the spins of these two electrons are parallel, they cannot share a common orbit because of the Pauli exclusion principle, so that they form separate orbits, thus reducing the Coulomb interaction [23].

For localized spins, the energy contribution is parametrized in the exchange interaction Hamiltonian [20]

$$\mathcal{H}_{\text{ex}} = -\sum_{i,j}^N J_{ij} \boldsymbol{S}_i \cdot \boldsymbol{S}_j = -2 \cdot \sum_{i>j}^N J_{ij} \boldsymbol{S}_i \cdot \boldsymbol{S}_j \, . \tag{2.6}$$

Due to the overlap of electronic orbitals, the interaction decreases rapidly with increasing distance and is described by Bethe-Slater function. For this reason, in theoretical considerations, the summation is sometimes limited only to nearest neighbours. In a continuum approach, the exchange energy density is written as

$$\epsilon_{\text{ex}} = \frac{A_{\text{ex}}}{V} \iiint_\Omega (\nabla \boldsymbol{M})^2 \, \mathrm{d}V \, , \tag{2.7}$$

where A_{ex} is the exchange stiffness.

2.2.3. Demagnetizing field energy

Demagnetizing field energy is a long range dipolar interaction between the magnetic moments, which describes Zeeman-like mutual interactions of all magnetic moments in a ferromagnet. The macrospin origin can be seen from the Maxwell's equations

$$\nabla \cdot \boldsymbol{B} = \mu_0 \nabla \cdot (\boldsymbol{H}_{\mathrm{dem}} + \boldsymbol{M}) = 0 \,, \tag{2.8}$$

$$\nabla \times \boldsymbol{H}_{\mathrm{dem}} = 0 \,. \tag{2.9}$$

The equation (2.9) is valid for zero free current density. Based on (2.8), it is possible to write $\boldsymbol{H}_{\mathrm{dem}}$ as the gradient of the scalar potential ϕ_{dem}:

$$\boldsymbol{H}_{\mathrm{dem}} = -\nabla \phi_{\mathrm{dem}} \,. \tag{2.10}$$

ϕ_{dem} fulfils Poisson's equation

$$\Delta \phi_{\mathrm{dem}} = -\varrho_M \,, \tag{2.11}$$

where ϱ_M is defined as $\varrho_M = -\nabla \boldsymbol{M}$ and represents a magnetic charge density. The solution of (2.11) is standard problem of classical electrodynamics, which can be solved by a Green's function approach [24, 25].

Doing so for a special case of a uniformly magnetized ellipsoid

$$\boldsymbol{H}_{\mathrm{dem}} = -\hat{N} \cdot \boldsymbol{M} \,, \tag{2.12}$$

where $\hat{N}$ is a demagnetizing field tensor, which depends on the geometrical shape of the sample. If the coordinate system is oriented along the principal axes of the ellipsoid, $\hat{N}$ is diagonal tensor

$$\hat{N} = \begin{pmatrix} N_x & 0 & 0 \\ 0 & N_y & 0 \\ 0 & 0 & N_z \end{pmatrix} \,. \tag{2.13}$$

In general case, the calculation of $\boldsymbol{H}_{\mathrm{dem}}$ is complicated, because $\hat{N}$ can be analytically found for only a few geometries.

In the continuum model, the demagnetizing field energy density is described by

$$\epsilon_{\mathrm{dem}} = -\frac{\mu_0}{2V} \iiint\limits_{\Omega} \boldsymbol{M} \cdot \boldsymbol{H}_{\mathrm{dem}} \mathrm{d}V \,. \tag{2.14}$$

When the demagnetizing field $\boldsymbol{H}_{\mathrm{dem}}$ is a linear function of the magnetization with the location-independent demagnetizing tensor $\hat{N}$, equation (2.14) can be expressed as

$$\epsilon_{\mathrm{dem}} = -\frac{\mu_0}{2} \boldsymbol{M} \cdot \hat{N} \cdot \boldsymbol{M} \,. \tag{2.15}$$

2.2.4. Anisotropy energy

Due to the lattice symmetries, a further energy contribution depends on the direction of the magnetization $\boldsymbol{M}$ relative to the structural axes of the material. The origin of this dependence is the sample shape and the spin-orbit interaction. It is described by the anisotropy energies. For a further reading, interested reader may consult references [21, 26, 27].

Symmetry plays huge role in description of anisotropies. Therefore, expansions in terms of spherical harmonics are often used to describe the most important contributions. For the sake of simplicity, we will restrict ourselves to example of a uniaxial anisotropy found in hexagonal and tetragonal crystals. The energy density of the uniaxial anisotropy is given by

$$\epsilon_{\text{uni}} = K_{\text{u}1} \sin^2 \vartheta + K_{\text{u}2} \sin^4 \vartheta + \dots , \tag{2.16}$$

where $K_{\text{u}i}$ are anisotropy constants and ϑ is angle between magnetization and anisotropy axis. Rarely more than the first two significant terms have to be considered, usually only the first is taken into account. There are even cases, where no term is considered, e.g. in Permalloy (Py) films, where random orientation of grains (crystallites) results in no net anisotropy.

In general, two cases are distinguished.

- $K_{\text{u}1} > 0$ – describes an easy axis. The energy is minimal, when the magnetization $\boldsymbol{M}$ is collinear.

- $K_{\text{u}1} < 0$ – describes an easy plane, which is perpendicular to the anisotropy axis and is called hard axis. The energy is maximal when the magnetization $\boldsymbol{M}$ and anisotropy axis are collinear, hence the magnetization tends to align perpendicular to it.

The total energy density ϵ_{tot} of the system is sum of all the individual contributions

$$\epsilon_{\text{tot}} = \epsilon_{\text{Z}} + \epsilon_{\text{ex}} + \epsilon_{\text{dem}} + \epsilon_{\text{uni}} . \tag{2.17}$$

The magnetic ground state of the magnetization might be determined by finding the minima in (2.17). Now we can introduce the total effective magnetic field $\boldsymbol{H}_{\text{eff}}$. It is defined as the functional derivative of ϵ_{tot} with respect to magnetization $\boldsymbol{M}$ as

$$\boldsymbol{H}_{\text{eff}} = -\frac{1}{\mu_0} \nabla_{\boldsymbol{M}} \epsilon_{\text{tot}} . \tag{2.18}$$

For equilibrium, $\boldsymbol{M}$ is parallel to $\boldsymbol{H}_{\text{eff}}$. When $\boldsymbol{M}$ is not parallel to $\boldsymbol{H}_{\text{eff}}$, $\boldsymbol{H}_{\text{eff}}$ represents the precessional axis of the magnetization.

2.3. Magnetization dynamics

In this section, a brief introduction to theory of magnetization dynamics is provided. The equation of motion governing the magnetization dynamics will be described. The complex dynamic susceptibility will be derived from the equation of motion.

2.3.1. Precession of moments

From a historical development of the concept of magnetism, rotating electric charge distributions have played an essential role. Before the discovery of spin, rotating electric charge distributions were held fully responsible for the magnetic moments of atoms and magnetization of solids [17].

For clarity it should be stressed, that the definition of magnetic moment $\boldsymbol{\mu} = p\boldsymbol{d}$ is based on imaginary magnetic charges p^+ and p^-, separated by a distance d.

When the magnetic field is homogeneous, the same magnitude of a magnetic field is experienced by the poles p^+ and p^- of a magnetic dipole. From a classical mechanics, it exerts an equal force $\boldsymbol{F} = p\boldsymbol{H}$ on each magnetic pole. The torque on a magnetic moment $\boldsymbol{\mu}$ in a field $\boldsymbol{H}$ is given by

$$\boldsymbol{T} = \boldsymbol{\mu} \times \boldsymbol{H} \,. \tag{2.19}$$

The torque causes the vector of the angular momentum $\boldsymbol{L}$ to move according to Newton's classical equation of motion $\mathrm{d}\boldsymbol{L}/\mathrm{d}t = \boldsymbol{T}$. Using (2.19) we obtain

$$\frac{\mathrm{d}\boldsymbol{L}}{\mathrm{d}t} = \boldsymbol{T} = \boldsymbol{\mu} \times \boldsymbol{H} \,. \tag{2.20}$$

The equation of motion of the magnetic moment $\boldsymbol{\mu}$ in a field $\boldsymbol{H}$ is given by

$$\frac{\mathrm{d}\boldsymbol{\mu}}{\mathrm{d}t} = -\gamma \left(\boldsymbol{\mu} \times \boldsymbol{H} \right) = \gamma \boldsymbol{T} \,, \tag{2.21}$$

where $\gamma = g|e|\mu_0/2m_e$ is the gyromagnetic ratio, choosing a convention of a positive γ. This leads to the Larmor precession of $\boldsymbol{\mu}$ around the magnetic field $\boldsymbol{H}$ at the angular frequency $\omega = \gamma H$.

The Larmor precession frequency can be derived from (2.21). The change $\mathrm{d}\boldsymbol{\mu}$ of the magnetic moment is perpendicular to both $\boldsymbol{\mu}$ and $\boldsymbol{H}$ [see Figure 2.1a)]. Therefore, $\boldsymbol{\mu}$ can only process around $\boldsymbol{H}$. If $\boldsymbol{\mu}$ is divided to the components, where $\mu_\perp$ is the component perpendicular to the $\boldsymbol{H}$ and $\mu_\parallel$ is the component parallel to the $\boldsymbol{H}$, then $\mathrm{d}\boldsymbol{\mu} = \boldsymbol{\mu}_\perp \times \mathrm{d}\boldsymbol{\varphi}$, where $\mathrm{d}\varphi$ is the angle of precession in the time interval $\mathrm{d}t$. Then simply $\frac{\mathrm{d}\boldsymbol{\mu}}{\mathrm{d}t} = \boldsymbol{\omega} \times \boldsymbol{\mu}_\perp$. The left hand side of (2.21) is $\gamma \mu_\perp H$, yielding the result $\omega = \gamma H$.
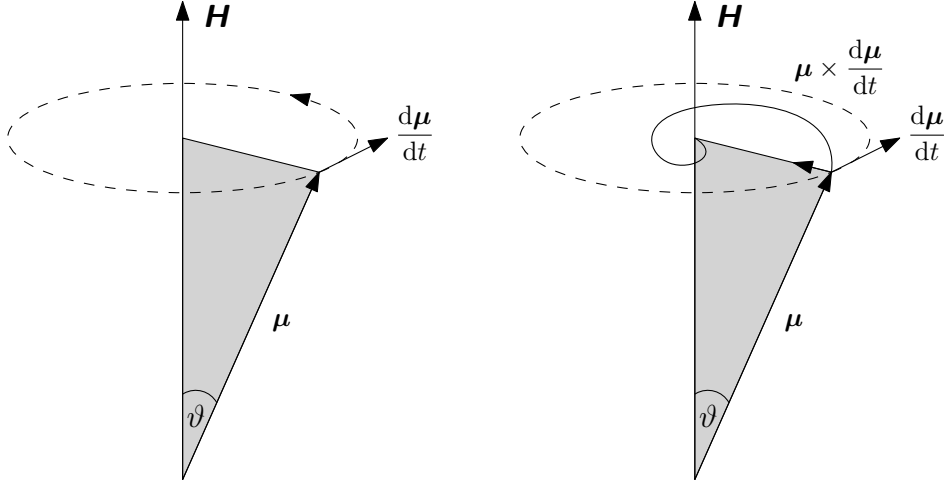

Figure 2.1: Magnetization precession. a) Without damping. b) With damping.

From the experience, we can tell that (2.21) is an idealized case where no damping term is included. In reality, additional torque must be introduced. This additional torque $\boldsymbol{T}_\mathrm{D}$ is perpendicular to the precessional torque and perpendicular to $\boldsymbol{\mu}$ and is called the damping torque. From Figure 2.1b) we can write

$$\boldsymbol{T}_\mathrm{D} = C \left[\boldsymbol{\mu} \times \frac{\mathrm{d}\boldsymbol{\mu}}{\mathrm{d}t} \right] \,, \tag{2.22}$$

where C is purely phenomenological constant of proportionality. In the constant C one might see the origin of the damping.

2.3.2. Landau-Lifshitz equation of motion

The effective magnetic field $\boldsymbol{H}_{\text{eff}}$ introduced in section 2.2.4 determines the static equilibrium orientation of the magnetization. For simplicity, in this section, $\boldsymbol{H} \equiv \boldsymbol{H}_{\text{eff}}$. For a continuum approach, we can replace the magnetic moment $\boldsymbol{\mu}$ with a magnetization $\boldsymbol{M}$. A realistic equation of motion for $\boldsymbol{M}$ is the *Landau-Lifshitz* (LL) equation [28]:

$$\frac{\partial \boldsymbol{M}}{\partial t} = -\gamma \left(\boldsymbol{M} \times \boldsymbol{H}\right) + \lambda \boldsymbol{M} \times \left(\boldsymbol{M} \times \boldsymbol{H}\right) . \tag{2.23}$$

Here, γ is the gyromagnetic ratio and λ is a phenomenological damping parameter. The most often employed damping term was derived by Gilbert [29]. Using this approach, the equation (2.23) becomes

$$\left(1 + \alpha_{\text{LLG}}^2\right) \frac{\partial \boldsymbol{M}}{\partial t} = -\gamma \left(\boldsymbol{M} \times \boldsymbol{H}\right) - \frac{\gamma \alpha_{\text{LLG}}}{M_{\text{s}}} \left[\boldsymbol{M} \times \left(\boldsymbol{M} \times \boldsymbol{H}\right)\right] , \tag{2.24}$$

where α_{LLG} is the Gilbert damping parameter and M_{s} is the saturation magnetization. The equation (2.24) is so-called *Landau-Lifshitz-Gilbert* (LLG) equation. For small α_{LLG}, the term α_{LLG}^2 is negligible. The LLG equation can also be written in slightly different form:

$$\frac{\partial \boldsymbol{M}}{\partial t} = -\gamma \left(\boldsymbol{M} \times \boldsymbol{H}\right) + \frac{\alpha_{\text{LLG}}}{M_{\text{s}}} \left(\boldsymbol{M} \times \frac{\partial \boldsymbol{M}}{\partial t}\right) . \tag{2.25}$$

The equivalence of (2.24) and (2.25) is proven in Appendix A.1.

2.3.3. Dynamic susceptibility

Finding an analytical solution for the LLG differential equation (2.25) is not possible in a general form. Therefore, we solve it for a special case under the following assumptions: [30]

- Sample is a thin film, which is infinitely extended in the xy plane. The demagnetizing factors are $N_x = N_y = 0$ and $N_z = 1$ [see equation (2.12)].

- Anisotropy fields are zero or neglected.

- A homogeneous magnetic field $\boldsymbol{H} = H\boldsymbol{e}_x$ is applied along the x-axis and the static magnetization is aligned with it. A small harmonic excitation field $\boldsymbol{h} = h\boldsymbol{e}_y \exp\left(\mathrm{i}\omega t\right)$ with angular frequency ω is applied along the y-axis The effective field is

$$\boldsymbol{H}_{\text{eff}} = \begin{bmatrix} H \\ h_y \exp\left(\mathrm{i}\omega t\right) \\ 0 \end{bmatrix} + \boldsymbol{H}_{\text{ex}} + \boldsymbol{H}_{\text{D}} . \tag{2.26}$$

- The dynamic component $\boldsymbol{m}$ of the magnetization is assumed to be small compared to the saturation magnetization $|\boldsymbol{m}| \ll M_{\text{s}}$.

- $\boldsymbol{m}$ depends harmonically on the time t and precession occurs around the x-axis. The total magnetization is

$$\boldsymbol{M} = \begin{bmatrix} M_{\text{s}} \\ m_y \exp\left(\mathrm{i}\omega t\right) \\ m_z \exp\left(\mathrm{i}\omega t\right) \end{bmatrix} . \tag{2.27}$$

Inserting all this into equation (2.25) and neglecting all quadratic terms of **M** or **H**, we get a linearised set of coupled differential equations [31], which reads [32]

$$(\omega_H + i\alpha_{\text{LLG}}\omega)\, m_y - i\omega m_z = \omega_M h_y\,, \tag{2.28}$$

$$i\omega m_y + (\omega_H + \omega_M + i\alpha_{\text{LLG}}\omega)\, m_z = 0\,, \tag{2.29}$$

where

$$\omega_H = \gamma H\,, \qquad\qquad \omega_M = \gamma M_{\text{s}}\,. \tag{2.30}$$

We can rewrite equations (2.28) and (2.29) in a matrix form as

$$\begin{bmatrix} \omega_H + i\alpha_{\text{LLG}}\omega & -i\omega \\ i\omega & \omega_H + \omega_M + i\alpha_{\text{LLG}}\omega \end{bmatrix} \begin{bmatrix} m_y \\ m_z \end{bmatrix} = \omega_M \begin{bmatrix} h_y \\ 0 \end{bmatrix}\,. \tag{2.31}$$

To extract the susceptibility tensor $\hat{\chi}$ after *Polder* [33], we need to create an inverse matrix to find

$$\begin{bmatrix} m_y \\ m_z \end{bmatrix} = \boldsymbol{m} = \hat{\chi}\boldsymbol{h} = \begin{bmatrix} \chi_{yy} & \chi_{yz} \\ \chi_{zy} & \chi_{zz} \end{bmatrix} \begin{bmatrix} h_y \\ 0 \end{bmatrix}\,, \tag{2.32}$$

leading to

$$\hat{\chi} = \frac{\omega_M}{\omega_H(\omega_M + \omega_H) - \omega^2 + i\omega\alpha_{\text{LLG}}(2\omega_H + \omega_M)} \begin{bmatrix} \omega_H + \omega_M + i\alpha_{\text{LLG}}\omega & i\omega \\ -i\omega & \omega_H + i\alpha_{\text{LLG}}\omega \end{bmatrix}\,. \tag{2.33}$$

The real and imaginary parts $\chi'_{yy} - i\chi''_{yy}$ (negative sign following common convention) are

$$\chi'_{yy} = \frac{\omega_M(\omega_H + \omega_M)\,(\omega_r^2 - \omega^2)}{(\omega_r^2 - \omega^2)^2 + \alpha_{\text{LLG}}^2\omega^2\,(2\omega_H + \omega_M)^2}\,, \tag{2.34}$$

$$\chi''_{yy} = \frac{\alpha_{\text{LLG}}\omega\omega_M\left[\omega^2 + (\omega_M + \omega_H)^2\right]}{(\omega_r^2 - \omega^2)^2 + \alpha_{\text{LLG}}^2\omega^2\,(2\omega_H + \omega_M)^2}\,, \tag{2.35}$$

where the field dependent resonance frequency ω_r is introduced

$$\omega_r^2 = \omega_H(\omega_M + \omega_H) = \gamma^2 H(H + M_{\text{s}})\,. \tag{2.36}$$

The field dependence of the resonance frequency of the arbitrary ferromagnetic body is described by (2.36), the so called Kittel formula [34]. For completeness, the other components of susceptibility tensor are listed:

$$\chi'_{yz} = -\chi'_{zy} = \frac{\alpha_{\text{LLG}}\omega\omega_M(2\omega_H + \omega_M)^2}{(\omega_r^2 - \omega^2)^2 + \alpha_{\text{LLG}}^2\omega^2\,(2\omega_H + \omega_M)^2}\,, \tag{2.37}$$

$$\chi''_{yz} = -\chi''_{zy} = \frac{\omega\,(\omega_r^2 - \omega^2)}{(\omega_r^2 - \omega^2)^2 + \alpha_{\text{LLG}}^2\omega^2\,(2\omega_H + \omega_M)}\,, \tag{2.38}$$

$$\chi'_{zz} = \frac{\omega_M\omega_H\,(\omega_r^2 - \omega^2)}{(\omega_r^2 - \omega^2)^2 + \alpha_{\text{LLG}}^2\omega^2\,(2\omega_H + \omega_M)^2}\,, \tag{2.39}$$

$$\chi''_{zz} = \frac{\alpha_{\text{LLG}}\omega\omega_M\,(\omega^2 + \omega_H^2)}{(\omega_r^2 - \omega^2)^2 + \alpha_{\text{LLG}}^2\omega^2\,(2\omega_H + \omega_M)}\,. \tag{2.40}$$

When $\omega = \omega_r$, χ_{yy} exhibits an extremal value. We call this value resonance of the uniform precessing magnetization, i.e. ferromagnetic resonance (FMR).

From FMR one can extract the resonance frequency for a magnetic thin film

$$f_r = \frac{\omega_r}{2\pi} = \frac{\gamma}{2\pi}\sqrt{H^2 + M_{\text{s}}H}\,. \tag{2.41}$$

2.4. Spin waves

In the preceding sections, we addressed uniform precession of magnetization. The LLG equation describes the magnetization dynamics in homogeneously magnetized structures, within the macro-spin approximation. At $T = 0\,\mathrm{K}$ a ferromagnet is perfectly ordered. If the temperature is increased, reduction of the magnetization is observed. If the temperature is above the critical temperature T_c, the magnetization vanishes. To explain the temperature dependence of the ferromagnetic materials, the concept of spin waves as collective excitations of magnetic moments in magnetically ordered materials was introduced by Bloch in 1929 [35]. When the temperature is significantly below T_c, low energy transverse fluctuations of the magnetization in ferromagnet are known as spin waves. In the analogy with lattice vibrations, spin waves are quantized in nature and their quanta are called magnons.

Spin waves (magnons) are collective oscillations of magnetic moments. Of particular interest regarding the propagation properties of spin waves is the characteristic dispersion relation, i.e. the dependence of angular frequency ω on wave vector k.

Spin wave frequencies are typically observed in the gigahertz range in so called dipolar spin wave regime, but can also reach the terahertz frequencies in exchange mediated spin waves [36]. The wavelengths are in the range of millimetre to the nanometre scale.

In this section, different types of spin waves in ultra-thin film samples will be discussed. The general formalism for spin waves in a thin film of thickness t will be provided.

Let the total wave vector $\boldsymbol{k}$ consists of an in-plane component $\boldsymbol{k}_\zeta$ and an out-of-plane component $\boldsymbol{k}_p$. Magnitude of k is given by

$$k^2 = k_\zeta^2 + k_p^2 \,. \tag{2.42}$$

The in-plane component k_ζ is decomposed in a component parallel to the magnetic field H, i.e. $k_\parallel$, and a component perpendicular to the magnetic field, $k_\perp$, by

$$k_\zeta^2 = k_\parallel^2 + k_\perp^2 \,. \tag{2.43}$$

The out of plane component k_p is quantized due to the geometrical constrain in the perpendicular direction

$$k_p = \frac{p\pi}{t} \,, \qquad p = 0, 1, 2, \dots \tag{2.44}$$

Based on the angle between the magnetization $\boldsymbol{M}$ and the in-plane component of the wave vector $k_\parallel$, the different magnetostatic modes are distinguished. Part of their naming is related to the dispersion relation of the modes, i.e. the frequency ω as a function of a wave vector k. Except for ω and k, the propagation properties of spin waves are also fully described by the knowledge of group v_g and phase v_{ph} velocities defined as

$$v_g = \frac{\partial \omega}{\partial k} \,, \qquad v_{ph} = \frac{\omega}{k} \,. \tag{2.45}$$

Modes, where the v_g and v_{ph} have the same direction, are called forward waves. Modes with opposite direction of v_g and v_{ph} are called backward waves. Figure 2.2 shows a typology for different orientations between the in-plane wave vector, $\boldsymbol{k}_\zeta$, and the magnetization $\boldsymbol{M}$. Three different geometries are shown.
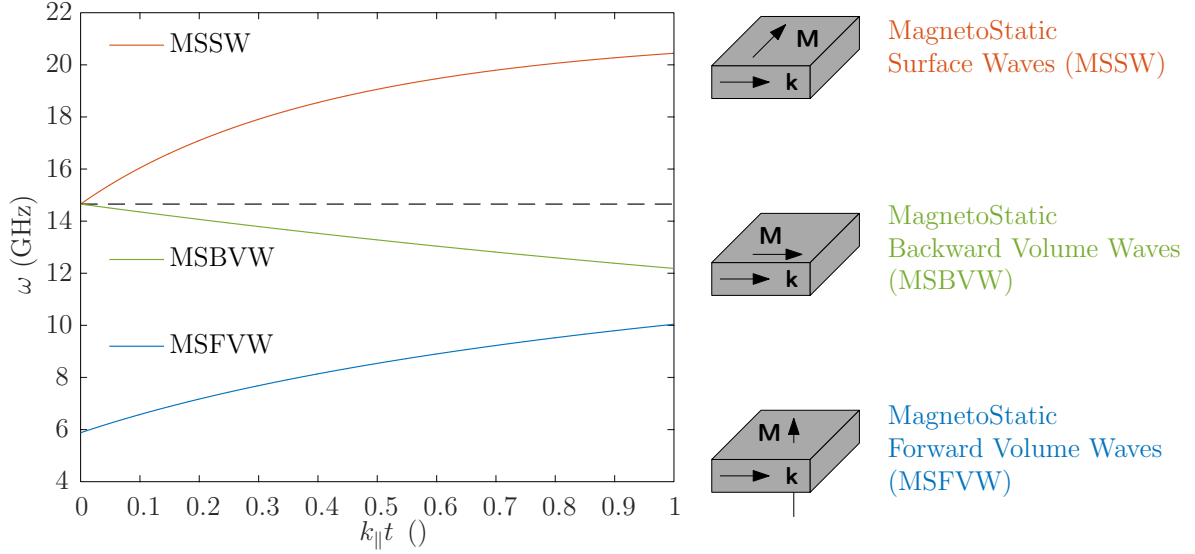
Figure 2.2: The dispersion relation and geometry for three magnetostatic modes calculated using (2.47), (2.48) and (2.49). The magnetization is aligned by an external field as illustrated in the sketch on the right hand side. Parameters are: $\mu_0 H = 200\,\mathrm{mT}$, $M_\mathrm{s} = 830\,\mathrm{kA/m}$, $t = 100\,\mathrm{nm}$.

2.4.1. Spin wave spectrum of magnetic wires

The calculation of a spin-wave spectrum of an axially magnetized infinite ferromagnetic wire with a rectangular cross section has never been solved analytically. Nevertheless, in the particular case of a thin wire with $t \ll w$, where w is width of the wire and t is its thickness, the calculation can be approximately done using the theory of a dipole exchange in a magnetic film [24].

The dipole exchange spin-wave spectrum in an infinite thin ferromagnetic film is described by the Herrings-Kittel formula [37]

$$f = \frac{\gamma \mu_0}{2\pi} \left[\left(H + \frac{2A_\mathrm{ex}}{\mu_0 M_\mathrm{s}} \left(\frac{p\pi}{t} \right)^2 \right) \left(H + \frac{2A_\mathrm{ex}}{\mu_0 M_\mathrm{s}} \left(\frac{p\pi}{t} \right)^2 + M_\mathrm{s} \right) \right]^{1/2}, \qquad (2.46)$$

where γ is the gyromagnetic ratio, A_ex is the exchange stiffness constant, see (2.7). H is the applied magnetic field, M_s is the saturation magnetization, t is a finite thickness and $p = 0, 1, 2, \dots$ is a quantization number for the so-called perpendicular standing spin waves (PSSW).

MagnetoStatic Surface Waves (MSSW)

The magnetostatic surface waves are also called Damon Eshbach modes, because they were first described by Damon and Eshbach in 1960 [38]. When the magnetization is in the sample plane and wave vector $\boldsymbol{k}_\parallel$ is perpendicular to $\boldsymbol{M}$, MSSW are observed. The phase and group velocities point in the same direction, thus this mode is a *forward wave*. The dispersion relation is given by [19]

$$\omega_\mathrm{MSSW}^2 = \omega_H (\omega_H + \omega_M) + \frac{\omega_M^2}{4} \left[1 - \exp(-2k_\parallel t) \right]. \qquad (2.47)$$

Thus, if the film is magnetized in-plane and $\boldsymbol{k}_\parallel \perp \boldsymbol{M}$, the spin-wave modes described by (2.42, 2.43, 2.44, 2.46) can be divided into the dipole-dominated surface mode ($p = 0$)

11

and exchange-dominated thickness- or perpendicular standing spin-wave (PSSW) modes ($p > 0$) [39].

Note that in the limit case $k_\parallel \to 0$, this corresponds to (2.36). The wave amplitude decays exponentially from the surfaces of the film to bulk. Because of this, the modes are called magnetostatic surface waves or surface spin waves.

MagnetoStatic Backward Volume Waves (MSBVW)

In these modes, the magnetization is in the sample plane and wave vector $\boldsymbol{k}_\parallel$ is parallel to $\boldsymbol{M}$. The phase and group velocities are pointing in opposite directions, thus this wave is called a *backward wave*. The dispersion relation is approximated as [24]

$$\omega^2_{\text{MSBVW}} = \omega_H \left[\omega_H + \omega_M \left(\frac{1 - \exp(-k_\parallel t)}{k_\parallel t} \right) \right] . \tag{2.48}$$

As for (2.47), for $k_\parallel \to 0$, uniform in-plane precession frequency (2.36) is found. The wave amplitude is distributed sinusoidally through the volume of the film. Hence, the designation of this mode.

MagnetoStatic Forward Volume Waves (MSFVW)

When the magnetization is perpendicular to the sample plane, these modes occur. An approximation of the dispersion relation has been derived by Kalinikos [40]

$$\omega^2_{\text{MSFVW}} = \omega_H \left[\omega_H + \omega_M \left(1 - \frac{1 - \exp(-k_\parallel t)}{k_\parallel t} \right) \right] . \tag{2.49}$$

Note that the wave propagation does not depend on the direction of the in-plane wave vector $\boldsymbol{k}_\parallel$ (this holds only in the absence of magnetocrystalline anisotropy). The phase and group velocities are both in the same direction, therefore this wave is called a *forward wave*. As in the case of MSBVW, the amplitude is uniformly distributed through the volume of the film.

2.5. Magnonic crystal

In this section, different types of magnonic crystals are described. The developed functional magnonic devices will be listed. The effect of periodic variation of different parameters in a magnetic film to form a magnonic crystal will be discussed.

In the 1960s and 1970s, spin waves (SW) in magnetic thin layers have attracted tremendous amount of interest. In the 1980s, the research focus has shifted towards magnetic superlattices [41]. These superlattices can be viewed as 1D magnonic crystals.

To realize various magnonic devices, it is most convenient to alter the properties of a single material. This microscopical manipulation is the reason of the success of the semiconducting materials such as silicon. These materials have a band gap at the Fermi level, therefore, no states are available for conducting in this region. Hence, for designing electronic properties, doping is necessary. In an analogous manner, photonic and magnonic materials can be designed.

Thus, magnonic crystals are the microwave, magnetic analogue of photonic and sonic crystals. At first, periodic magnetic structures were used in microwave filters, resonators

and generators [42]. Periodically altered magnets and creation of artificial band structure is approachable in many ways. In Figure 2.3, the modification of spin-wave eigenfrequency and band structure is illustrated either by sample thickness [43] or by two materials with different saturation magnetization [44].
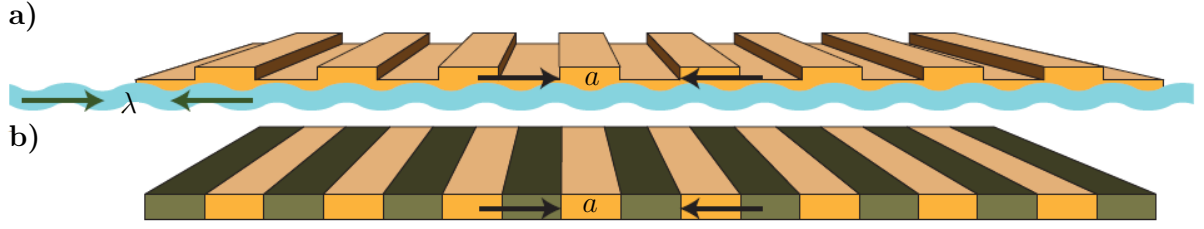

Figure 2.3: **a)** Periodic variation of the thickness of a homogeneous material (orange) and **b)** an alternating sequence of two different magnetic materials (orange and green) results in stop bands and artificial band structures for spin waves (cyan). Adapted from [45].

Figure 2.4 shows magnonic crystal consisting of the spatially separated nanomagnets.
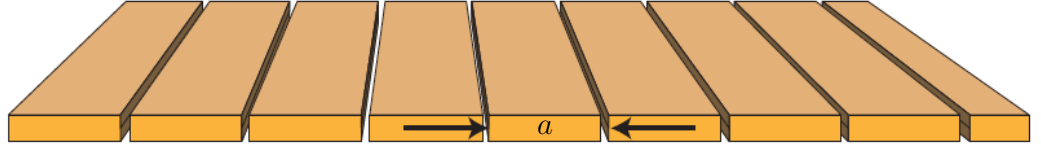
Figure 2.4: Periodic air gaps of microscopic width give rise to the tailoring of the spin-wave band structure. Adapted from [45].

Spin dynamics is governed by either static (applied field, demagnetization field) or dynamic (stray field from precession, applied microwave field) magnetic fields. A tunable magnonic crystal is illustrated in the Figure 2.5. A periodically modulated magnetic field is in this case produced by applying a current to a meander-type conductor [46].
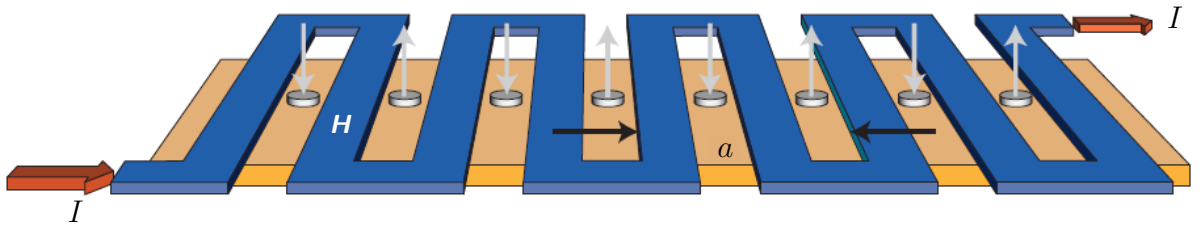
Figure 2.5: The magnetic field **H** induced by a current I from a conductor (blue strip) induces a periodically alternating internal magnetic field. In this type of a dynamic magnonic crystal band structure, specifically band widths depend on I. Adapted from [45].

In Figure 2.6 there is a sketch of selectively reversed magnetic moments. Within this configuration, the period is not fixed by the geometry, but is reprogrammable via different magnetic states.

Chumak *et al.* [47] experimentally demonstrated frequency band gaps in magnonic crystal. The results are depicted in Figure 2.7. The spin waves are excited by the microwave antenna, which is placed across Py waveguides and detected by the space-resolved Brillouin light scattering microscopy [48]. The bias magnetic field is applied across the
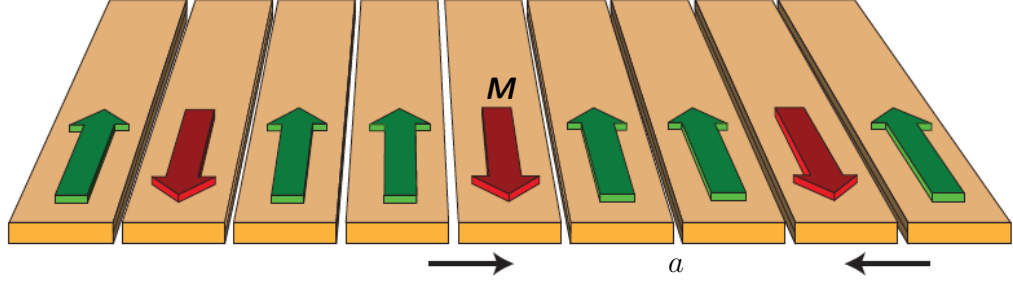
Figure 2.6: Magnonic crystal with a reconfigurable structure consisting of bistable nanostrips. The directions of magnetization vectors (large arrows) are selectively varied to change both wavelengths λ at which signal transmission is haltered and the number of allowed minibands. Adapted from [45].

waveguide, see Figure 2.7a). The lowest fundamental width mode calculation of dispersion of a 2.5 μm-wide uniform waveguide is shown in Figure 2.7b) as solid line. For comparison, as a dashed line, the dispersion for a 1.5 μm-wide uniform waveguide is shown. In Figure 2.7c) a red dotted line denotes the experimentally measured SW intensity for the reference waveguide as a function of the applied microwave frequency. Solid blue line depicts the measured intensity for the magnonic crystal. For frequencies close to 8 GHz, a rejection band, where spin waves are not allowed to propagate is clearly found. The calculated SW intensity is in very good agreement with the experiment [see dashed blue line in Figure 2.7c)]. The transmission characteristic for the magnonic crystal for different bias magnetic fields is presented in Figure 2.7d). The agreement between the theory and the experiment is observed. The variation of the applied bias magnetic field in the range from 15 mT to 70 mT allows to control the band gap frequency in the range from 6.5 GHz to 9 GHz.
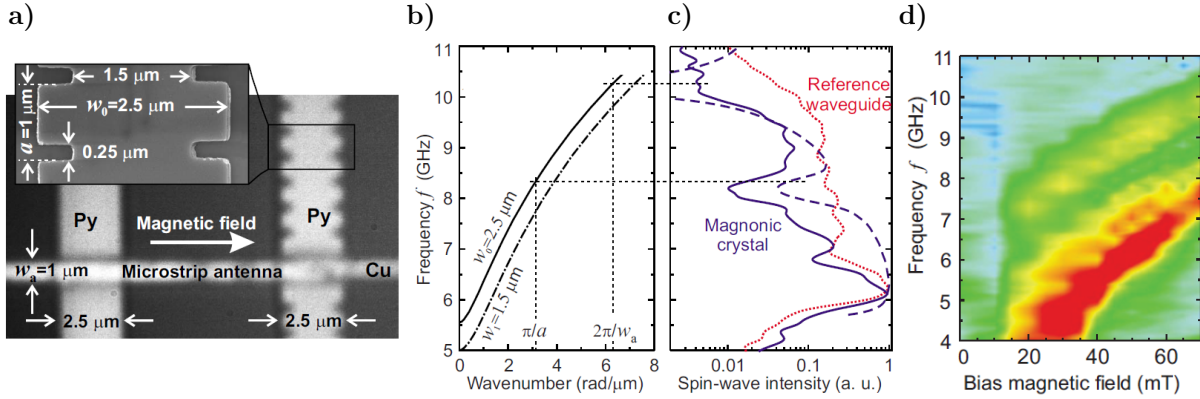

Figure 2.7: a) Scanning electron microscopy and optical images of the magnonic crystal. **b)** Calculated dispersion curves for uniform waveguides. **c)** Measured normalized SW intensity as a function of the applied microwave frequency. **d)** Measured SW intensity as a function of frequency and bias magnetic field. Red corresponds to the maximum and blue to the minimum SW intensity. Adapted from [47].

2.5.1. Magnonic devices

There are many advantages magnonic devices can offer. In this paragraph, the properties that challenge the main technologies in terms of the further miniaturization of

reprogrammable GHz electronics are stressed. The future beyond complementary metal-oxide-semiconductor (CMOS) technology lies in the substitution of electrons by photons or magnons. The advantage is based on using operations with vector rather than scalar variables. Information can be encoded in the amplitude or phase of the spin waves (SW) [49]. The usage of a wave phase opens the way to non-Boolean computing algorithms [50]. The wavelength of the used wave defines the minimal sizes of wave-based computing elements. SWs allow operations with wavelengths below 10 nm. Other advantage is the wide frequency range from GHz to THz, because the wave frequency defines the maximum clock rate of a computing device.

Nowadays, the subject of intensive theoretical and experimental studies are the standard logic operations with digital binary data. The first attempt to use logic gates based on spin waves made use of Mach–Zehnder spin wave interferometer equipped with current-controlled phase shifters embedded in the interferometer arms to construct logic gates [51].

In Figure 2.8 there is a proof-of-principle XNOR logic gate realized by Schneider *et al.* [52]. Logic inputs are represented by currents applied to Input 1 and Input 2. The 'on' state, corresponding to logic '1', results from a π-phase shift of the spin wave in the respective interferometer arm; 'off' state corresponds to logic '0'.
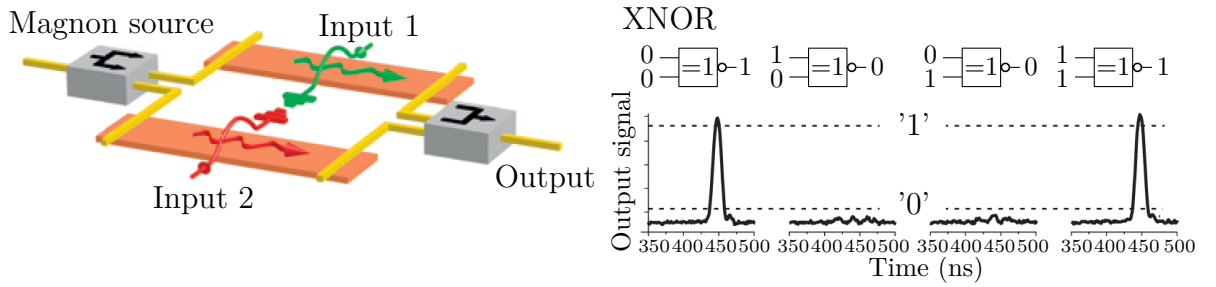

Figure 2.8: Spin wave XNOR logic gate using Mach-Zender interferometer with current-controlled phase shifters [52].

An alternative design of nanometre-sized logic gate have been proposed by Lee *et al.* [53], see Figure 2.9. In this device, a nanowire, placed at the centre of the interferometric device, is controlling the SWs via a d.c. current. The d.c. current defines the logic input and amplitude of the output SW defines the logic output.
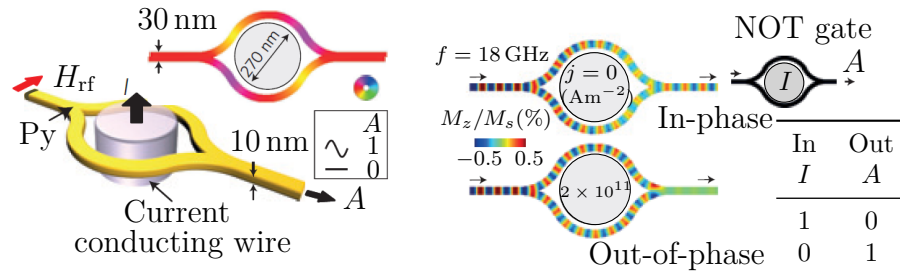

Figure 2.9: Spin wave NOT logic gate using an alternative design of Mach-Zender interferometer. The simulation corresponds to two different d.c. currents [53].

Proposal by Khitun *et al.* [49] deals with digitizing information using the SW phase instead of SW amplitude. Via this approach, majority logic gate in the form of a multi-input SW combiner might be realized (Figure 2.10).

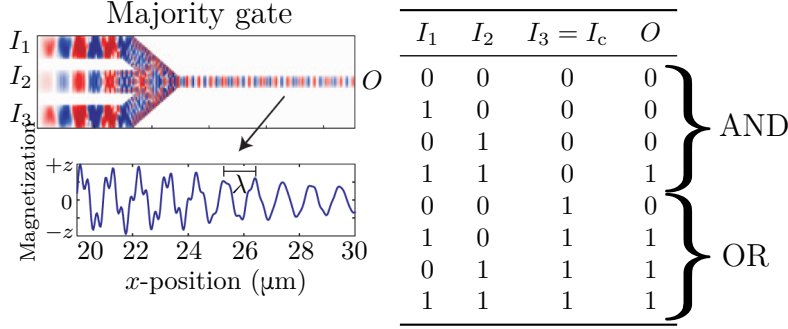| I_1	I_2	$I_3 = I_c$	O	
0	0	0	0	
1	0	0	0	
0	1	0	0	AND
1	1	0	1	
0	0	1	0	
1	0	1	1	
0	1	1	1	OR
1	1	1	1	

Figure 2.10: Majority gate operating with data coded into spin-wave phase. The colour map represents the amplitude of the spin wave for the case of equal input phases. The majority gate can perform OR and AND logic operations [54].

2.6. Thermoelectric essentials

Theoretical fundamentals of thermoelectric and thermomagnetic effects have been known for two centuries [55], nevertheless the technology of fabrication of samples reinvigorated the field. The first of the thermoelectric effects was discovered in 1821 by T. J. Seebeck [56]. The Seebeck effect evidenced when connecting two wires of different metals, e.g. copper and iron. Once the other ends of the wires are connected to the sensitive voltmeter and the junction between the wires is heated, the small voltage is measured by the voltmeter.

Thirteen years after Seebeck, the second of the thermoelecric effects was observed by J. C. Peltier [57]. He found that depending on the direction of the passage of an electric current through a thermocouple, either a small heating or cooling is produced. The Peltier effect is always accompanied by the Joule heating effect, and is quite difficult to demonstrate using metallic thermocouples.

The interdependency of the Seebeck and Peltier effects was recognised by W. Thomson (who later became Lord Kelvin), in 1851 by applying the theory of thermodynamics to the problem [58]. This approach showed the existence of the third thermoelectric effect in a homogeneous conductor, the Thomson effect.

The practical Peltier refrigerators were introduced only in the 1950s, when the semiconductors as thermoelectric materials were introduced. Unfortunately, from the time of the introduction of semiconductor elements there was a slight improvement in thermoelectric materials [59].

Assume a temperature difference ΔT between the two junctions and that free ends of the conductor are maintained at the same temperature. The differential Seebeck coefficient is then defined as

$$S = \frac{V}{\Delta T}\,, \tag{2.50}$$

where V is the potential difference between the free ends. The expression of the Peltier coefficient in terms of the Seebeck coefficient is

$$\Pi = ST\,. \tag{2.51}$$

2.6.1. Effects in a magnetic field

When a magnetic field is applied, the thermoelectric effects, together with other transport properties, are changed. Under the influence of the magnetic field, the Seebeck and Peltier coefficients are changed. The modified relation gives

$$\Pi(B) = TS(-B) \, . \tag{2.52}$$

Current carrying conductor in the presence of a perpendicular magnetic field develops an electric field perpendicular to both the current and magnetic field. This effect was discovered in 1879 by Edwin Hall [60]. The transverse voltage arises due to the Lorentz force

$$\boldsymbol{F} = e(\boldsymbol{E} + \boldsymbol{v} \times \boldsymbol{B}) \tag{2.53}$$

acting on the moving electrons [60]. The generated (Hall) voltage is proportional to the applied magnetic field. The effect is known as Hall effect. However, in magnetic metals, he found that the transverse voltage is not proportional to the applied magnetic field [61]. This effect came to be known as the anomalous Hall effect (AHE). The AHE has been an enigmatic problem that has resisted theoretical and experimental assaults for almost a century [62]. Experimentally, it was investigated that the Hall resistivity ϱ_{H} initially increases steeply in weak B but saturates at a large value that is nearly B independent (see Fig. 2.11). An empirical relation between ϱ_{H}, B, and M established in [62–64] states

$$\varrho_{\mathrm{H}} = R_{\mathrm{o}}B + \mu_0 R_{\mathrm{a}}M \, , \tag{2.54}$$

where R_{o} is the ordinary Hall coefficient and R_{a} is the anomalous Hall coefficient (sometimes extraordinary Hall coefficient). The ordinary Hall coefficient R_{o} tends to be fairly temperature independent, whereas R_{a} is usually very temperature dependent. The AHE is not only seen in ferromagnets, but also in strong antiferromagnets or paramagnets [15].
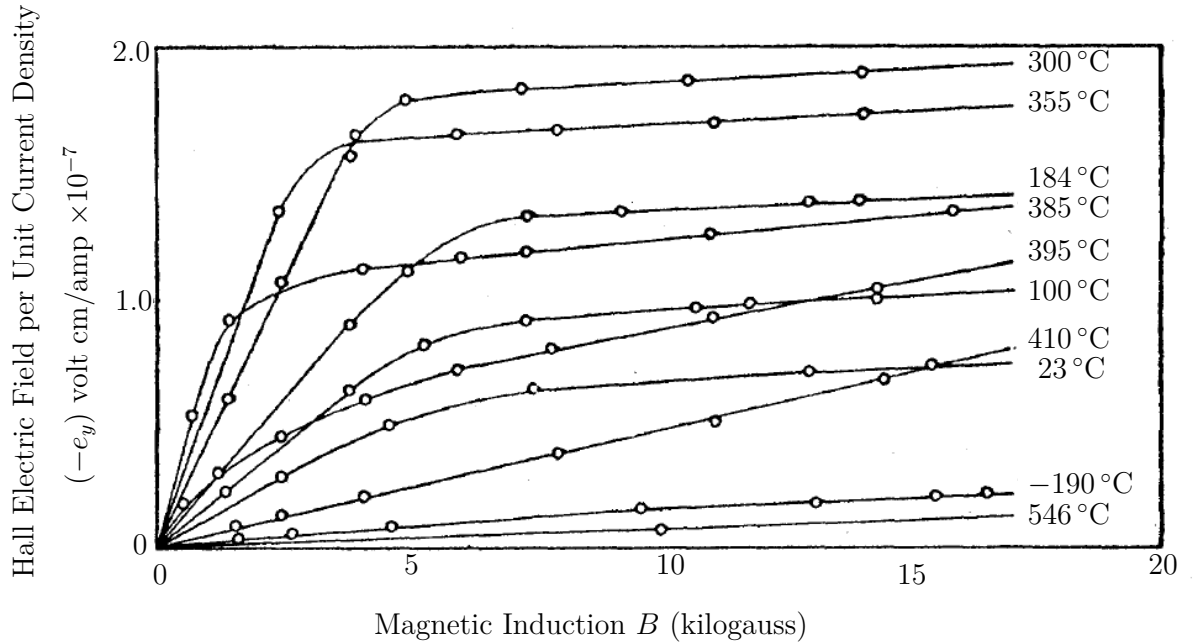

Figure 2.11: The anomalous Hall effect in Ni. Adapted from [64, 65].

2. BASIC THEORY OF MAGNETIZATION DYNAMICS

The Hall and anomalous Hall effects are not directly connected with the energy conversion, but are useful, when explaining charge carriers behaviour. Effects relevant to the energy conversion are the transverse Nernst and Ettingshausen effects.

The Nernst effect describes the generation of a transverse electric field E_y in a magnetic field B_z, but unlike the Hall effect, which depends on a longitudinal electric field, the Nernst effect depends on the longitudinal temperature gradient $\nabla_x T$.

The Nernst coefficient is given by

$$|N| = \frac{E_y}{B_z \nabla_x T} \,. \tag{2.55}$$

Figure 2.12 illustrates the sign of the Nernst coefficient, and all the transverse thermogalvanomagnetic effects. In contrast to the Hall effect, the sign of Nernst effect does not depend on the type of charge carriers (positive or negative). The relation between Etting-
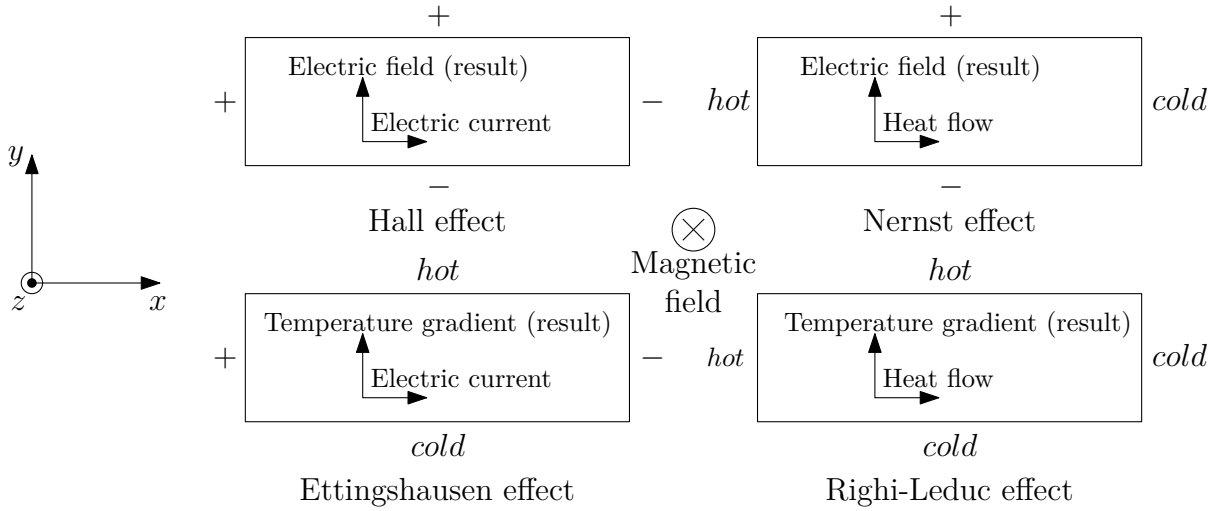
Figure 2.12: Thermogalvanomagnetic effects. Figure describes effects with the positive coefficient. Adapted from [59].

shausen and Nernst effects is analogous to the relation between the Peltier and Seebeck effects. The Ettingshausen effect describes a generation of a transverse temperature gradient as a result of a transverse magnetic field and a longitudinal flow of electric current. The Ettingshausen coefficient is defined by

$$|P| = \frac{\nabla_y T}{i_x B_z} \,, \tag{2.56}$$

where i_x is the longitudinal current density.

As expected the thermodynamic relationship between the Nernst and Ettingshausen coefficients is given by

$$P\lambda = NT \,, \tag{2.57}$$

where λ is the thermal conductivity.

To complete the list of tranverse effects, the Righi-Leduc effect should be mentioned. The Righi-Leduc effect represents the transverse temperature gradient induced by a longitudinal heat flow. The Righi-Leduc coefficient is given by

$$|R| = \frac{\nabla_y T}{B_z \nabla_x T} \,. \tag{2.58}$$

Table 2.1: Classical spin-independent galvanomagnetic and thermomagnetic transport phenomena.

Phenomenon	Applied	Measured
Hall effect	I_x, B_z	E_y
Nernst effect	$\nabla_x T$, B_z	E_y
Ettingshausen effect	I_x, B_z	$\nabla_x T$
Righi-Leduc effect	$\nabla_x T$, B_z	$-\nabla_y T$

The spin-independent transport coefficients are summarized in Table 2.1. Spin caloritronics (from 'calor', the Latin word for heat) is a field that emerged in its current form only after the discovery of the spin Seebeck effect (SSE) in 2008 [66]. Due to the interaction between spin, charge, and heat currents, it has attracted interest in the research community. The main focus of spin caloritronics is the interaction of spins with heat currents [11, 12].

2.6.2. Anomalous Nernst effect

In normal metals in the presence of external magnetic field, thermal Hall effects exist [class (iii)] and can be divided into three groups [67]. The Hall voltage induced by a heat current is represented by the Nernst effect. The Ettingshausen effect describes the heat current that is induced transverse to an applied charge current. The Righi-Leduc effect represents the Hall heat current induced by a temperature gradient [68], see Figure 2.12.

To describe effects in normal metals, label 'spin' may be added, i.e. spin Hall effect, spin Nernst effect etc. In ferromagnets, two configurations might be distinguished. First, where magnetization is perpendicular to both currents (anomalous Hall effect (AHE), anomalous Nernst effect (ANE) and so on) and second configuration with in-plane magnetization (planar Hall effect [69], planar Nernst effect [70, 71] and so forth).

Compared to Nernst coefficient, see (2.55), in the ANE, an additional term, analogous to AHE, appears:

$$\frac{E_y}{\nabla_x T} = N\mu_0 H_z + N_A \mu_0 M_z\,. \tag{2.59}$$

In Figure 2.13, a sketch of the anomalous Nernst effect in a ferromagnetic film is depicted.
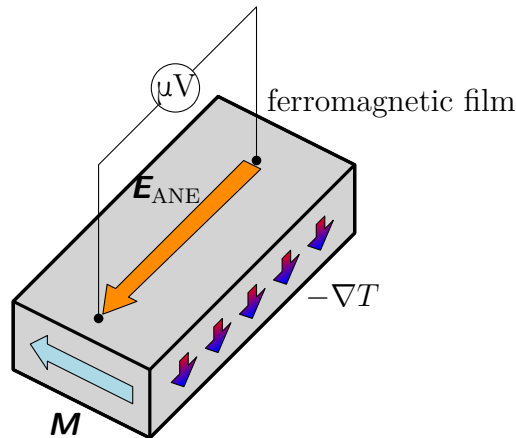
Figure 2.13: Schematic illustration of the anomalous Nernst effect.

2. BASIC THEORY OF MAGNETIZATION DYNAMICS

The deeper analysis of the microscopic origin of the ANE has not been done in the same details as in the case of AHE. There are some speculations, that at least in metals, the various Nernst effects might be related to the energy derivative of their equivalent Hall effects in the same way as the thermopower is related to the energy derivative of the conductivity by the Mott relation [72].

The anomalous Nernst effect in a conductive ferromagnetic thin film results in an electric field and is expressed as [73]

$$\boldsymbol{E}_{\mathrm{ANE}} = -N\mu_0 \boldsymbol{M} \times \nabla T \,, \tag{2.60}$$

where N is the Nernst coefficient.

3. Methods & Instrumentation

This chapter deals with the nanofabrication capabilities, sample design and techniques, used in the challenging preparation of the functional magnonic waveguides with active response in the frequency domain.

3.1. Electron beam lithography

The very versatile electron beam lithography (EBL) technique can provide very high resolution down to 10 nm [74–76]. On the other hand, due to its serial character it is time-consuming, particularly for large patterned areas. Figure 3.1 briefly shows basic lithography steps.
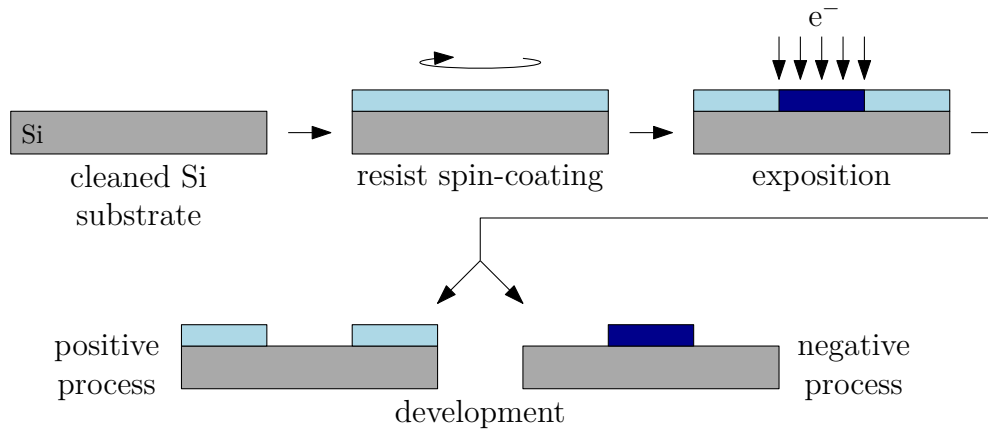
Figure 3.1: The scheme of a lithographical process. A resist is spin-coated onto a cleaned Si substrate and creates a homogeneous layer. An exposition by electrons is done in scanning electron microscope (SEM). The sample is then developed using special chemical treatment. Depending on type of resist spin-coated on the sample, the process is either positive or negative. With kind permission adapted from [77].

A droplet of resist is dropped on top of a cleaned Si substrate using a pipette. The substrate is spin-coated and the droplet of resist forms a layer. The sample is then locally irradiated with electrons in the scanning electron microscope (SEM). The development is done using special chemical treatment. There are two types of resists one can use.

1. In the positive process, the resist is a positive-tone, so the parts exposed throughout exposition step are dissolved during development. The resist used in a positive process is e.g. poly(methyl methacrylate) (PMMA).

2. The negative process uses a negative-tone resist and the parts exposed throughout exposition step remain during development. In the negative process one can use e.g. AR-N 7520.

The fabrication of the samples was done in Nanofabrication laboratory, which is part of CEITEC Nano. Resist used in the range of thesis were manufactured by Allresist GmbH[1].

The further processing of patterned substrates is described in the following sections. Reader interested in EBL might consult further details in literature [78, 79] or in bachelor's and master's thesis previously defended at the Institute of Physical Engineering, Brno University of Technology (IPE BUT) [77, 80]. In the range of this thesis Scanning Electron Microscope/E-beam writer TESCAN MIRA3/RAITH LIS was used for EBL. The instrument is equipped with the laser interferometer stage (LIS) to oppose the stage inaccuracy of common SEM, which is the key limitation for most lithography patterning.

3.2. Lift-off

The further processing of EBL patterned structures is most commonly done by lift-off technique. In the previous section, the description of EBL was provided. At the end of the EBL process, there is a substrate with a patterned resist layer on top of it. As it is shown in the Figure 3.2 in the lift-off process, the material of interest is either sputtered or evaporated onto the sample. In the range of this thesis Electron beam evaporator BESTEC[2] and ultra high vacuum (UHV) magnetron sputtering system BESTEC were used to deposit the material of interest on top of the patterned resist structures. Reader interested in the sputter deposition or evaporation techniques is encouraged to consult literature [81, 82].
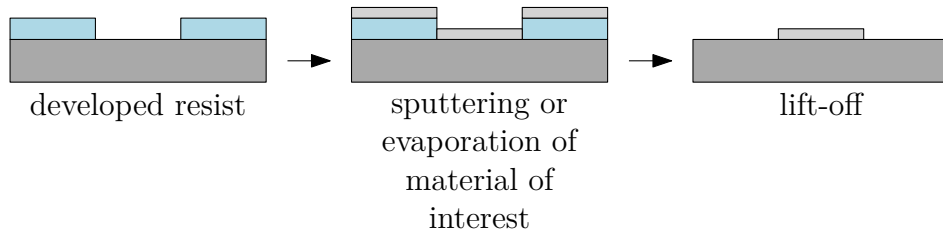

developed resist → sputtering or evaporation of material of interest → lift-off

Figure 3.2: Illustration of the lift-off process. Material of interest is either sputtered or evaporated onto the substrate with resist. The layer of resist is then dissolved in a resist remover (for PMMA it is acetone) and washed away along with the material on top of it either using squeeze bottle or ultrasonic agitation.

The layer of resist as well as the material deposited on top of it is then stripped and only the desired pattern remains on the substrate. For the most common positive e-beam resist, poly(methyl methacrylate) (PMMA), the solvent is acetone. In the case of negative e-beam resist, AR-N 7520, the propylene glycol monomethyl ether acetate (PGMEA) is the solvent.

---

[1]Allresist GmbH, http://www.allresist.com.
[2]BESTEC GmbH, http://www.bestec.de.

3.3. Experimental setup

Spin-wave (SW) excitations in ferromagnetic material usually cover the GHz frequency range. There are many ways how to excite and detect SWs. The most common ways how to induce SWs is either by current pulses [83], or by optical pulses [84, 85]. The detection of SWs is done by several techniques such as vector network analyser ferromagnetic resonance (VNA-FMR) [30], all electrical spin-wave spectroscopy (AESWS) [86], magneto optical Kerr effect (MOKE) [87], or Brillouin light scattering (BLS) [36]. More exotic technique uses local heating due to relaxation of SW energy to the phonon lattice, i.e. detection via thermoelectric effect [13]. In the scope of this thesis, the excitation of the SWs was done via microwave antenna (waveguide) and measurement of the response of the magnonic crystals was done via thermoelectric effect. The main components of the experimental setup are illustrated in Figure 3.3.
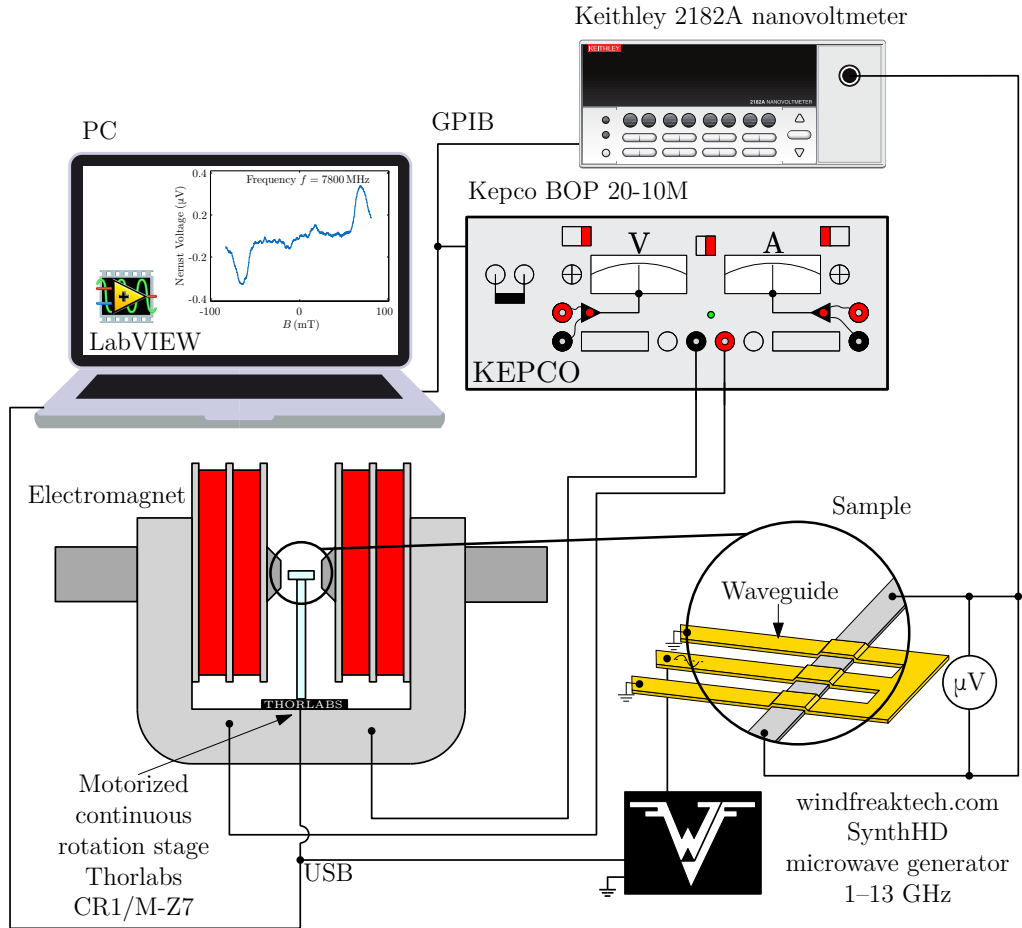
Figure 3.3: Sketch of the experimental setup. The sample is placed on the motorized continuous rotation stage Thorlabs CR1/M-Z7 in the electromagnet. Waveguide is connected via high frequency SMA (SubMiniature version A) connectors to the Windfreak SynthHD microwave generator and the magnetic sample via wires to the Keithley 2182A nanovoltmeter. The nanovoltmeter and the bipolar current source Kepco BOP 20-10M are connected to a computer via GPIB interface. The microwave generator and motorized rotation stage are connected to the computer via USB interface. The whole experiment was controlled by LabVIEW program.

3. METHODS & INSTRUMENTATION

The sample was located between the yokes of an electromagnet powered by the bipolar current source Kepco BOP 20-10M[3]. The electromagnet consists of a parallel pair of current coils and the iron core forming a closed loop magnetic circuit with an air gap. Two iron pole pieces are attached to increase generated magnetic field $\boldsymbol{H}$. The electromagnet produces field $\mu_0 H \leqq 2\,\mathrm{T}$ with $I = 20\,\mathrm{A}$. For the purposes of the work, field of the amplitude $\mu_0 H \leqq 0.1\,\mathrm{T}$ was used. The magnetic field in the electromagnet was calibrated using teslameter F. W. Bell 6010[4]. The microwave generator Windfreak Synth HD[5] was connected to a coplanar waveguide (CPW) using coaxial cables with SMA connectors to excite spin waves with $k \approx 0$. The sample was also connected with Keithley 21820A nanovoltmeter[6]. The sample holder with sample was fixed on the motorized continuous rotation stage Thorlabs CR1/M-Z7[7]. All cables were protected from bending and moving, because only a slight contact or movement might negatively influence the measurement. Additionally, the sample in the electromagnet was covered by aluminium foil to reduce the noise measured by nanovoltmeter.

National Instruments LabVIEW 2016 programme was designed with the help of Lukáš Flajšman & Marek Vaňatka to fully control the Windfreak SynthHD microwave generator, the bipolar current source KEPCO BOP 20-10M and Keithley 2182A nanovoltmeter. The current source and the nanovoltmeter were commanded using general purpose interface bus IEEE-488 (GPIB), and the microwave generator and motorized stage were controlled using universal serial bus (USB).

Coplanar waveguide design

In order to study the spin waves, they have to be excited first. To achieve this, the excitation via a coplanar wave guide (CPW) was chosen as the most convenient method. The CPW fabricated on a dielectric substrate was first demonstrated by C. P. Wen in 1969 [88]. The CPW is a structure for guiding a high frequency electromagnetic wave on a substrate. It is unique in its uniplanar construction, which implies that all of the conductors are on the same side of the substrate. This attribute simplifies manufacturing and allows fast and inexpensive characterization using on-wafer techniques [89]. In the range of this thesis, the CPW with finite ground lines is used. The CPW consists of three parallel electrically conducting lines, see Figure 3.4a). The width of the outer conductors (OCs), denoted as the ground lines, is w_{oc}, the inner conductor (IC) in between the ground lines is denoted as signal line with a width w_{ic}. The CPW is a symmetric structure, with respect to the inner conductor. The distance between the centre conductor edge and the outer conductor edge is denoted as s_{icoc}. The thickness of the CPW is t_{CPW}. The CPW comprise a wider part, suitable for wire-bonding to the chip and a thinner part. The excitation region with micrometre-sized dimensions, where the spin waves are excited in a ferromagnetic sample, is situated in the thinner part of the CPW.

Through the IC, a rf-current can flow and create a magnetic field. This field can be calculated in the magnetostatic approximation by the Biot-Savart's law:

$$\boldsymbol{B} = \frac{\mu_0}{4\pi} \int\limits_V \frac{(\boldsymbol{j}\mathrm{d}V) \times \boldsymbol{r}}{|\boldsymbol{r}|^3},\qquad(3.1)$$

---

[3]Kepco, Inc., http://www.kepcopower.com.
[4]Bell Technologies Inc., https://www.fwbell.com.
[5]Windfreak Technologies, LLC, https://www.windfreaktech.com.
[6]Tektronix, Inc., http://www.tek.com.
[7]Thorlabs, Inc., https://www.thorlabs.com.

where $\boldsymbol{j}$ is the current density. In the assumption of homogeneous current and infinitely long conductors, the field distribution can be calculated analytically.
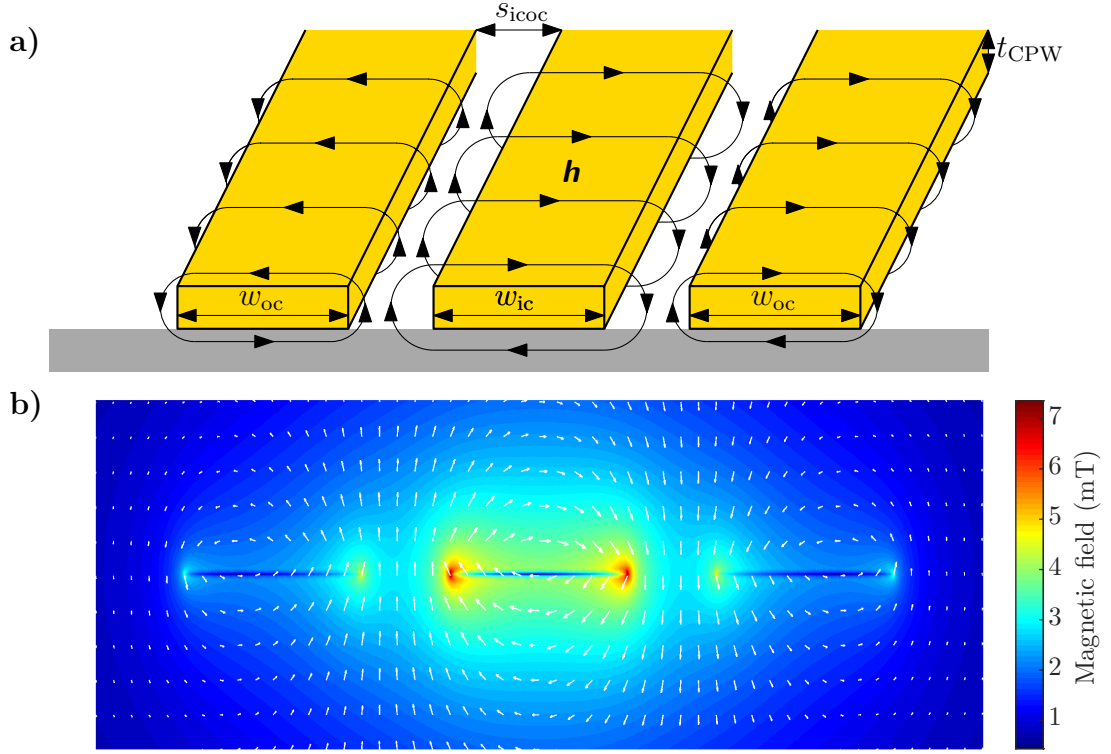

Figure 3.4: Schematic of the coplanar waveguide design. **a)** CPW consist of two outer conductors (OC) and one inner conductor (IC) in parallel. The width of the inner conductor is w_{ic} and the widths of the outer conductors are w_{oc}. The thickness of the CPW is t_{CPW}. s_{icoc} denotes the distance between the centre conductor edge and the outer conductor edge. The small harmonic excitation field $\boldsymbol{h}$ [see (2.26)] is approximately uniform and parallel to the surface of the conductor. **b)** Micromagnetic simulation of the magnetic vector field orientation and magnitude done in Finite Element Method Magnetics (FEMM). The parameters of simulation are: $w_{ic} = w_{oc} = 10\,\mu m$, $s_{icoc} = 5\,\mu m$ and $t_{CPW} = 100\,nm$. The current in the inner conductor is $I = -0.06\,A$ and the current in the outer conductors is $I = 0.03\,A$.

The currents in the OCs flow oppositely to the current in the IC and are half the magnitude of the current flowing in the ICs. Therefore, the in plane excitation field h_y^{rf} varies spatially. Vlaminck and Bailleul [90] showed, that the Fourier transform of the microwave current density $\xi(y)$ directly yields the wave vector distribution $\varrho(k)$. A very good approximation of the normalized current density is given by $h_y^{rf}(OC)/h_0 = -0.5$ and $h_y^{rf}(IC)/h_0 = 1$, normalized on the maximal field value h_0. The Fourier transform then gives the wave vector distribution $\varrho(k) \propto \mathcal{F}(h_y^{rf})$.

In Figures 3.5a), b) the calculated in-plane component of the magnetic field for a height of 200 nm above the waveguide together with the discrete fast Fourier transformation of $h_y(x)$ is depicted. The line profile was calculated by Lukáš Flajšman in FEMM[8] software. The FFT corresponds to the excitation spectrum $\varrho(k)$. A maximal value of $\varrho(k)$ is detected for $k = 0.29 \cdot 10^4\,rad/m$, which is the wave vector for which SW are most prominently excited by the CPW. In Figure 3.5b), there is the calculated dispersion relation for MSSW modes [see (2.47) and Figure 2.2]. For comparison, in Figure 3.5c), there is the dispersion

---

[8]Finite Element Method Magnetics, http://www.femm.info.
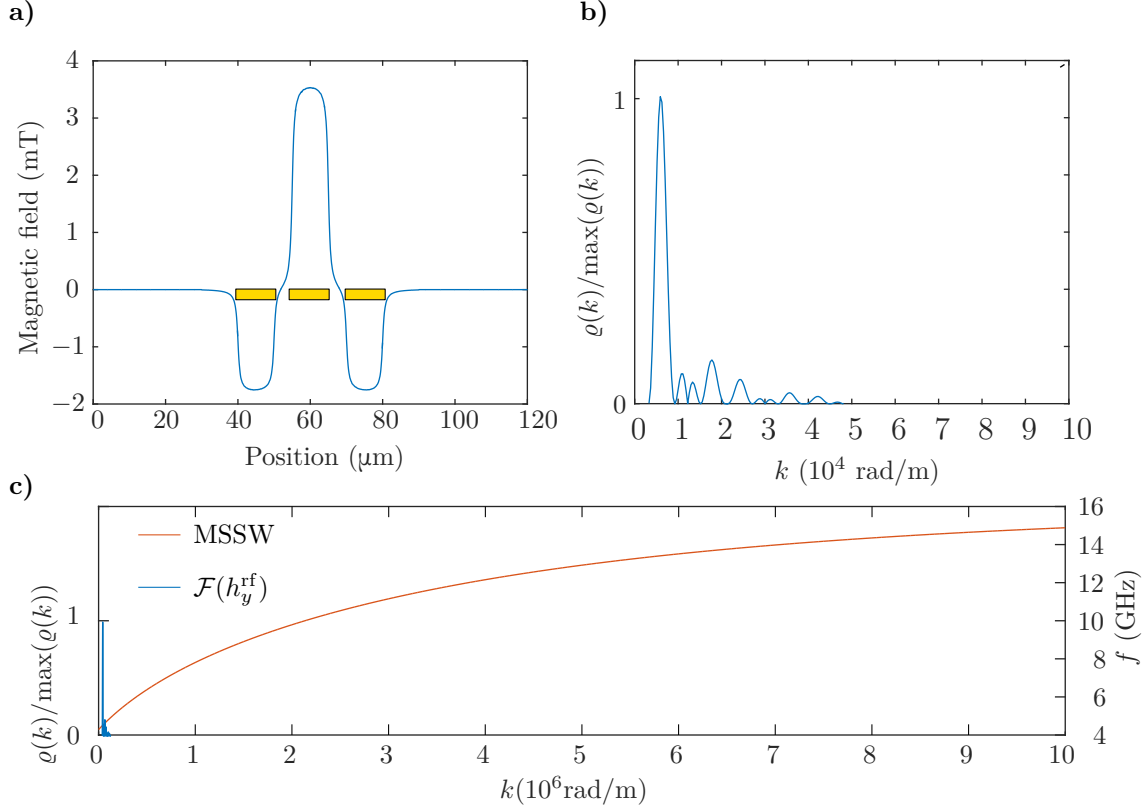
a)

b)

c)

Figure 3.5: a) Field plot of the spatial dependence of in-plane component of the microwave field $\mu_0 h_y^{\mathrm{rf}}$ obtained from the electromagnetic field simulations using the same parameters as described in the case of Figure 3.4b). Only the spatial distribution is of significance. **b)** Fourier transform of the spatial variation of h_y^{rf}. The wave vector for which $\varrho(k)$ is maximal is $k = 0.29 \cdot 10^4 \, \mathrm{rad/m}$. **c)** The dispersion relation for magnetostatic surface waves (MSSW). Parameters are: $\mu_0 H = 20 \, \mathrm{mT}$, $M_{\mathrm{s}} = = 830 \, \mathrm{kA/m}$ and $t = 100 \, \mathrm{nm}$.

for higher values of wavevector k. It is clearly seen, that by the waveguide, used in the range of the thesis, only spin waves with $k \approx 0$ are excited.

4. Sample fabrication

In this chapter fabrication of coplanar waveguides (CPW) and ferromagnetic wires is presented.

Two sets of samples were fabricated using electron beam lithography (EBL), see Section 3.1. The first set of samples consists of samples fabricated using three-step lithography. The second set of samples is prepared employing only one-step lithography.

4.1. Sample design

In Figure 4.1, a sketch of a sample is depicted. A typical sample consists of a substrate, a ferromagnetic strip, an insulator electrically insulating the ferromagnetic wire from the CPW, and the CPW. In the range of thesis, NiFe and Co were used as ferromagnetic wires. Already mentioned two sets of samples differ in a way of using different number of substrates and are also different in number of lithographical steps. The set of samples fabricated using one step lithography process consist of two substrates. A CPW and an insulation layer are located on the first one, and ferromagnetic strip is on the other one. For the sake of experiment, the two samples are put on top of each other. The set of samples fabricated using three step lithography process consist of only one substrate, where ferromagnetic strip, insulation layer and CPW are directly on top of each other.
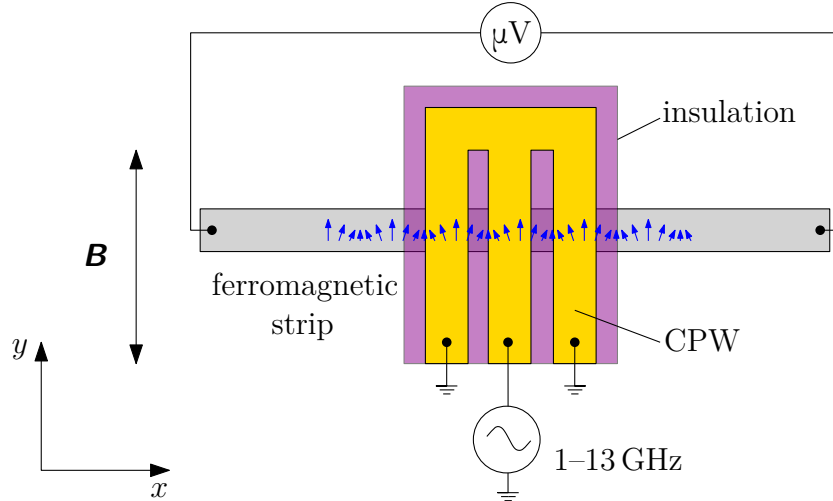

Figure 4.1: The not to scale sketch of sample under investigation. The ferromagnetic wire is 1.4 mm long and 20 μm wide. The thickness of the wire is between 50–150 nm. The CPW for spin wave excitation and the pads for d.c. voltage measurements are made from 100 nm thick Cu, covered with 20 nm of Au. The CPW has a signal linewidth of $w_{ic} = w_{oc} = 10$ μm and a signal-to-ground-line separation of $s_{icoc} = 5$ μm.

4.2. Preparation of samples

Samples were fabricated using methods described in detail in Chapter 3, such as EBL, deposition by e-beam evaporation or dc magnetron sputtering, and lift-off. The steps of preparation were as follows:

1. The substrates were cleaned in acetone and isopropyl alcohol (IPA) baths under ultrasonic agitation.

2. Prior to any process, substrates were etched for 5 min inside the Diener NANO Plasma Cleaner[1] by a 80:20% Ar:O_2 plasma.

3. A layer of poly(methyl methacrylate) (PMMA – in the Allresist terminology resit AR-P 679.04[2]) was spin-coated at 4000 RPM for 60 s onto the substrates using a spin-coater SÜSS LabSpin[3]. Post bake was done for 90 s at 150 ℃.

4. The sample was exposed in an area exposure mode to electrons in a scanning electron microscope TESCAN MIRA3/RAITH LIS[4,5]. Acceleration voltage was 20 kV, dose 240 μC/cm^2. Write field size was 400 μm. For the structure layout, KLayout[6], published under GNU General Public License[7], and commercial software ELPHY Plus[8] were used.

5. The exposed structures were developed for 3 min using AR-600-56[9]. The development was followed by an isopropyl alcohol (IPA) bath, duration 30 s.

6. To increase the adhesion and also to remove residues of resist, sample was etched for 1 min in the Diener NANO Plasma Cleaner (same conditions as in step 2.).

7. For deposition of materials, Electron beam evaporator[10] and High vacuum magnetron sputtering[11] were used. The e-beam evaporator with base pressure of $1 \cdot 10^{-8}$ mbar was used for deposition of NiFe and magnetron sputtering with base pressure of $5 \cdot 10^{-9}$ mbar, and working argon pressure of $5 \cdot 10^{-3}$ mbar was used for deposition of Co.

8. Lift-off was achieved by using acetone for 2 h and ultrasonic agitation. The sample was then washed with IPA and blow-dried with nitrogen.

These 8 steps formed the first step in multi-step EBL, see Figure 4.2. The second step in the three-step lithography process consisted of the following procedures:

1. A resist layer (AR-N 7520.17) was spin-coated at 4000 rpm for 60 s onto the sample using the spin-coater described in the first lithographic step. Post bake was done for 60 s at 85 ℃.

---

[1]Diener electronic GmbH, http://www.plasma.com.
[2]Allresist GmbH, http://www.allresist.com.
[3]SÜSS MicroTec AG, http://www.suss.com.
[4]TESCAN ORSAY HOLDING, a.s., http://www.tescan.com.
[5]Raith GmbH, http://www.raith.com.
[6]KLayout 0.24.9 by Matthias Köfferlein, Munich, http://www.klayout.de.
[7]GNU GPL, http://www.gnu.org.
[8]Raith GmbH, http://www.raith.com.
[9]Allresist GmbH, http://www.allresist.com.
[10]BESTEC GmbH, http://www.bestec.de.
[11]BESTEC GmbH, http://www.bestec.de.

2. E-beam exposure was done in an area exposure mode using the same SEM as in the first lithographic step. The acceleration voltage was $20\,kV$, dose $50\,\mu C/cm^2$ and write field size was $400\,\mu m$. Used resist is the negative type of resist (difference in using positive and negative resist is shown in the Figure 3.1).

3. Development of exposed structures was done using AR 300-47 for $50\,s$. Sample was then rinsed with deionized water (DI-H_2O).

4. The sample was hard-baked for $1\,min$ at $220\,°C$. The hard-baking was essential to ensure the durability of the resist in the next processing.

With this, the second lithographical step is accomplished. The third lithographical step consisted of almost the same procedures as the first lithographical step with the difference in material deposition. In this step, the e-beam evaporator was used to prepare the CPW and electrical contacts, located at the end of ferromagnetic strip to detect voltages generated along the strip. The CPW and electrical contacts are made from evaporated Ti ($10\,nm$), Cu ($100\,nm$) and Au ($20\,nm$).
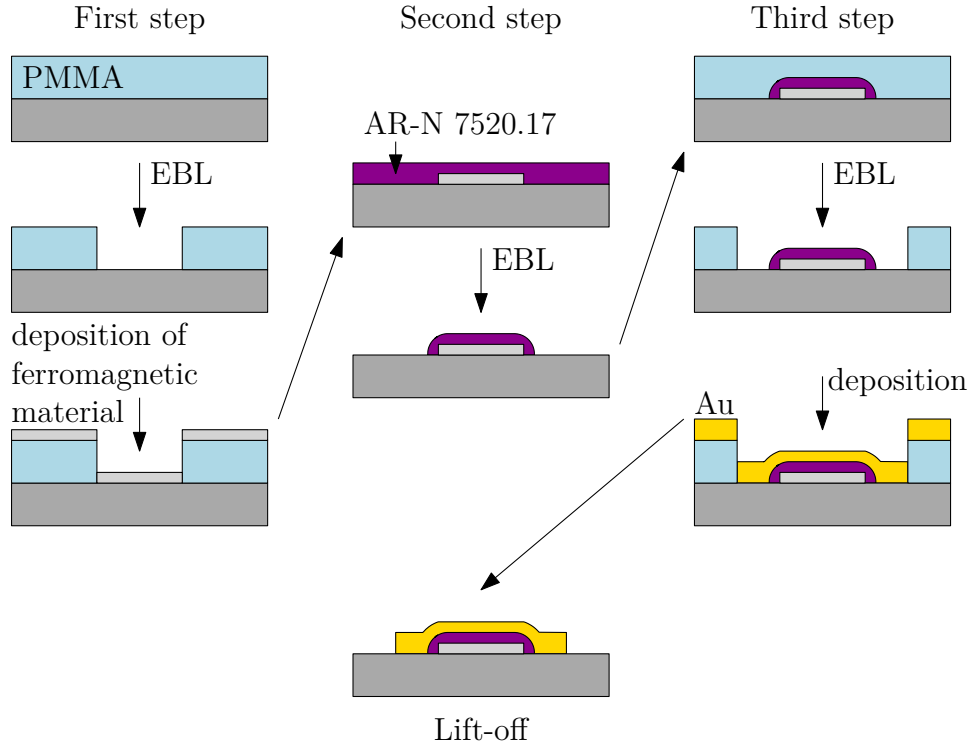
Figure 4.2: Process flow of a multistep EBL process. Accurate alignment is achieved by using local aligning marks.

Chemical cleaning of the substrate as well as plasma etching prior to any process was crucial to maintain the entire process without any harm to the sample. When steps of chemical cleaning or plasma etching were skipped prior to lithographic procedure, it resulted in destruction of the sample during second lithographical step. The main component of the developer AR 300-47 is tetramethylammonium hydroxide (TMAH) which in this case under-etched the NiFe strips. The result is shown in the Figure 4.3a). NiFe strips were not any more on the substrate, but rolled in various shapes and directions. This completely spoiled the whole process of sample preparation and resulted in even higher requirements of cleanness of substrate.

4. SAMPLE FABRICATION

In the Figure 4.3b), a not to scale sketch of the sample is shown. After the lithographical process, sample was glued to the home-made printed circuit board (PCB), which was drilled and milled using LPKF ProtoMat E44[12]. The sample was then wire-bonded to the PCB to establish the electrical connections to the chip, using ultrasonic wire bonder TPT HB 16[13].
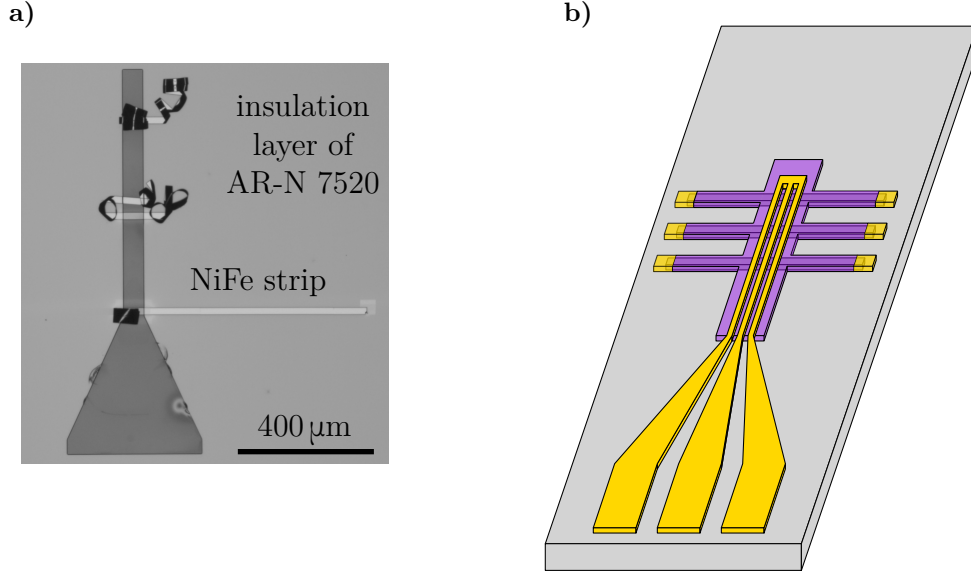

a)

insulation
layer of
AR-N 7520

NiFe strip

400 μm

b)

Figure 4.3: a) The optical microscope image of a destroyed sample after second step of the three-step lithography. The brighter parts are NiFe strips. The darker part is the negative resist AR-N 7520.17. The sample was spoiled because it was not cleaned enough prior to the procedures in the first lithographical step. The main component of the developer of negative resist (AR 300-47) is tetramethylammonium hydroxide (TMAH). In this case TMAH under-etched the NiFe strips, which resulted in strips rolled in various shapes. This led to even higher requirements of cleanness of substrate. **b)** The not to the scale sketch of the sample prepared using three-step lithography. The CPW comprises a wider part, suitable for wire-bonding to the chip and a thinner part, which excites the spin waves in a ferromagnetic strip. The CPW as well as electrical contacts, located at the end of ferromagnetic strip to detect voltages generated along the strips are fabricated in the last lithographical step.

In the Figure 4.4a), the optical microscope image of a typical, successfully prepared sample is depicted. To put the sample in the electromagnet and on the rotation stage (described in Section 3.3) special components were created from duraluminium and using 3D printed parts, see Figure 4.4b). In the case of 3D printing, Prusa i3 3D printer[14] was used.

When the multiple-step lithography was avoided by dividing the active components of experiment (excitation waveguide/antenna, insulation layer, probed sample) into two samples, as shown in Figure 4.4c), the same process of sample fabrication was used. Using this approach, the CPW was glued and wire-bonded to the one chip and the ferromagnetic strip was glued and wire-bonded to the second chip.

---

[12]LPKF Laser & Electronics AG, http://www.lpkf.com.

[13]TPT Wire Bonder, http://www.tpt-wirebonder.com.

[14]Prusa Research s.r.o, http://www.prusa3d.com.
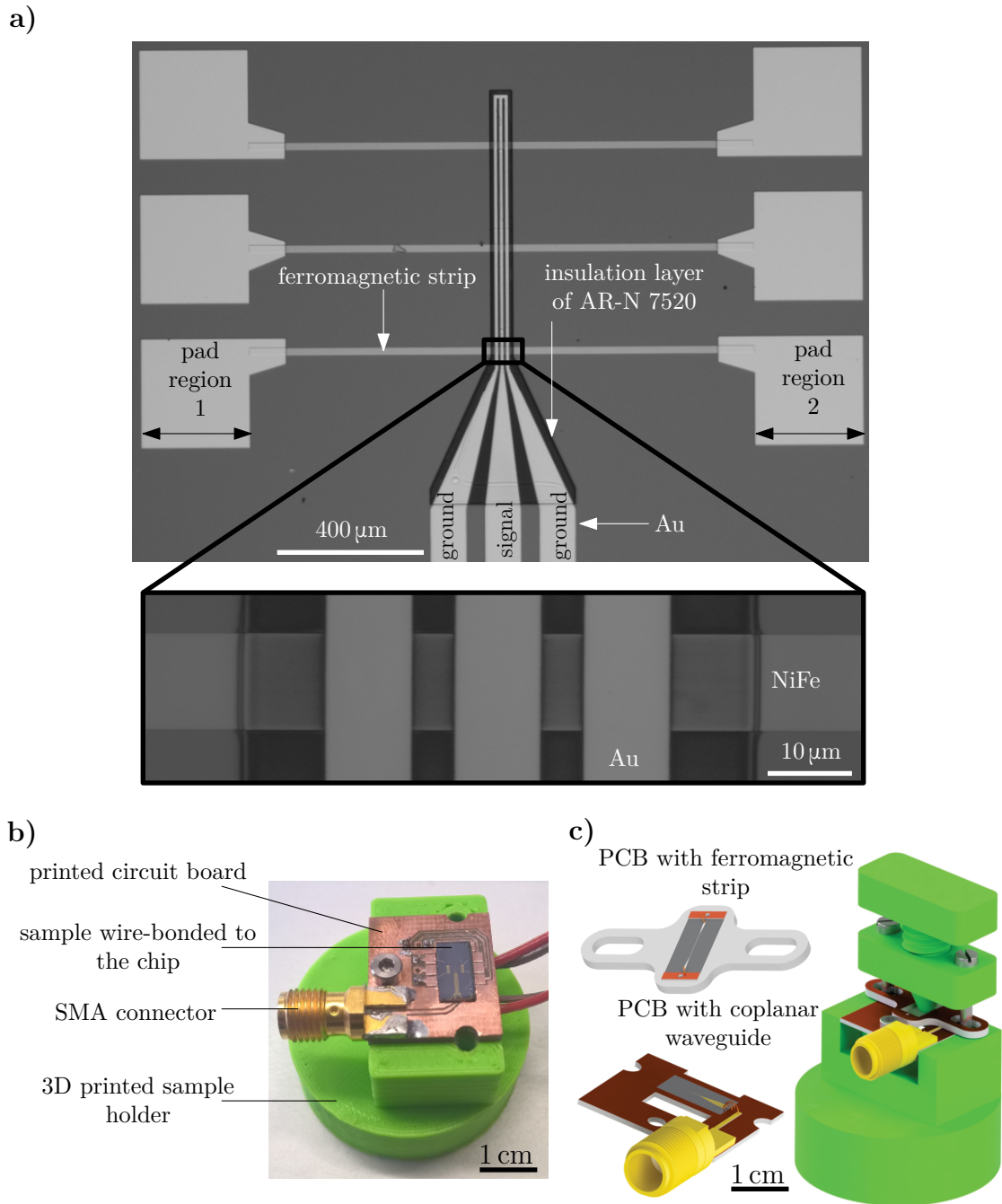
a)

b)

c)

Figure 4.4: a) The optical microscope image of a fabricated sample. The thin film coplanar waveguide (CPW) comprises a metallic signal line with two ground lines on either side. The CPW is referred to as SW emitter. The CPW is wire-bonded to the chip and connected to the microwave current generator. Perpendicular to the CPW there are NiFe wires with Au pads which are also wire-bonded to the chip. The voltage measured on the NiFe wires is the Nernst voltage. Between CPW and NiFe wire there is an insulation layer of AR-N 7520. **b)** A photograph of the sample, wire bonded to the PCB and screwed to the 3D printed sample holder, which was placed in the electromagnet and used for the measurements. **c)** The 3D model designed in Autodesk Inventor Professional 2017 of the sample holder and two PCBs, used in measurement with two samples placed on top of each other.

4.3. Patterned sample

In the range of the thesis, patterned sample, which played role of a magnonic crystal was fabricated. It was prepared using the procedure described in detail in Section 4.2. In Figure 4.5a), there is the optical microscope image of a first lithographical step, in which notched Py strip was fabricated. The dimensions of prepared magnonic crystal are depicted in Figure 4.5b). The width of the 100 nm thick strip varies periodically between 20 µm and 10 µm. The length of the wide and narrow sections is 0.5 µm. This forms a magnonic crystal with a lattice constant $a = 1$ µm. The final sample after three-step lithography is shown in Figure 4.5c).
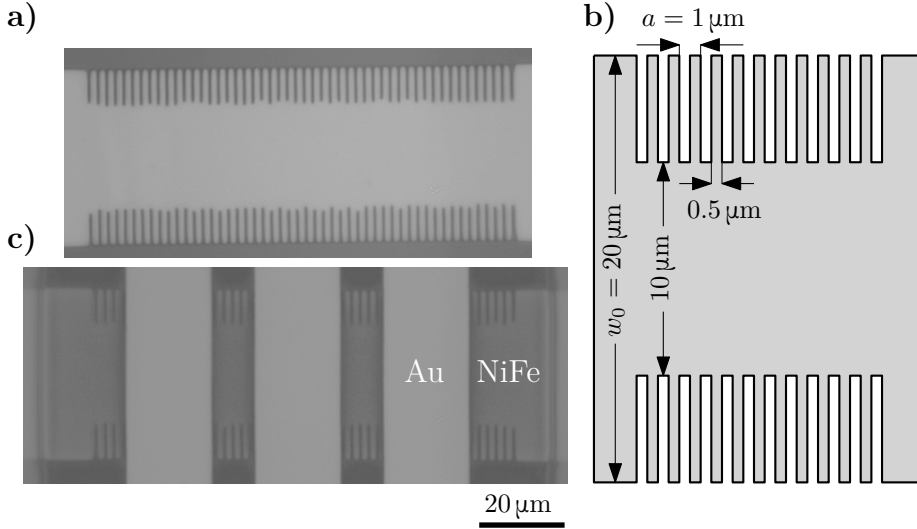
Figure 4.5: a) The optical microscope image of a Py magnonic crystal. **b)** Dimensions of the magnonic crystal. **c)** Finished sample with an excitation waveguide placed on top of the magnonic crystal.

4.4. Problems encountered in fabrication

The most challenging segment of the experimental part of the thesis was to successfully fabricate the samples using three step lithography (described in Section 4.2). Another demanding part was to wire-bond the samples to the printed circuit board (PCB).

Ferromagnetic materials used in the range of the thesis to fabricate the strips were NiFe and Co. The thicknesses of fabricated NiFe wires were $t_{NiFe} = 50, 100, 150$ nm. The thickness of Co strips was $t_{Co} = 100$ nm.

The encountered difficulties concerned e.g. problems with alignment of the lithographical steps, stitching failure or dirtiness of the sample. The misalignment was resolved by precise alignment in the first lithographical step, where global marks are fabricated. In other lithographical steps these marks were used to align coordinate system. Stitching difficulties were prevented by adjustment of write fields and sample layout in the KLayout and ELPHY software. The dirtiness of sample caused severe problems with wire-bonding. After a serious struggle, samples were fabricated and wire-bonded to the chip. The measurement was executed in the experimental setup, described in Section 3.3.

5. Results

This chapter is dedicated to the achieved experimental results. In the following sections, first, the experiment itself will be described. Second, the analysis of experimental results will be covered.

5.1. Measurement

The method we utilize for detection of spin-wave excitations aims for the simplification of the characterization experiment. We employ the thermoelectric detection of spin waves in magnetic strips via anomalous Nernst effect (see Section 2.6.2).

The experiment started with NiFe wires. The sample was in a static external magnetic field $\boldsymbol{B}$, which was applied perpendicular to the ferromagnetic strips (sample design described in detail in Section 4.1). For spin-wave (SW) excitation, the dynamic magnetic field $\boldsymbol{h}$ was applied by microwave currents using coplanar waveguide (CPW), see section 3.3. For this configuration, the torque $\boldsymbol{M} \times \boldsymbol{h}$ on the magnetization $\boldsymbol{M}$ is maximal and allows efficient excitations of spin waves with frequencies up to 13 GHz. Spin waves propagate along the x direction (see Figure 4.1) of the ferromagnetic strip and are attenuated in the material. For this configuration and these frequencies, the decay length of spin waves in Permalloy (Py), nickel iron magnetic alloy, is in the order of tens of micrometres [13, 83, 91–93]. As a result, the microwave energy, transferred from the CPW to the SWs is dissipated. The relaxation of spin waves to the lattice leads to the local heating of the Py strip. A local temperature gradient ∇T towards the substrate (perpendicular to the surface) is created due to the contact with Si substrate, which acts as a heat sink. This leads to generation of an electric field due to anomalous Nernst effect, perpendicular to both the temperature gradient and the magnetization direction, see Figure 2.13. The voltage is usually in the μV range, hence it can be measured with common laboratory equipment.

At the given constant excitation frequency, the static external magnetic field $\boldsymbol{B}$ was swept in the y direction, see Figure 4.1. In Figure 5.1a) a typical spin-wave spectrum is shown. The measurement was done at the frequency $f = 7800$ MHz. The measured voltages show distinct resonance peaks and change sign upon reversal of the field direction.

The Nernst voltage generated at the ends of ferromagnetic strip was measured as a function of the external magnetic field for frequencies from 1 GHz to 13 GHz in 50 or 100 MHz steps. The maps obtained during this measurement for NiFe and Co strips, fabricated using multi-step lithographical process are presented in Figures 5.2a–c). The map created using two samples [CPW and NiFe wire, see Figure 4.4c)] is shown in the Figure 5.2d).

When the response of magnonic waveguide to the SW excitation is measured, it is crucial to know the input, i.e. how the spin waves are excited in the ferromagnetic strip.
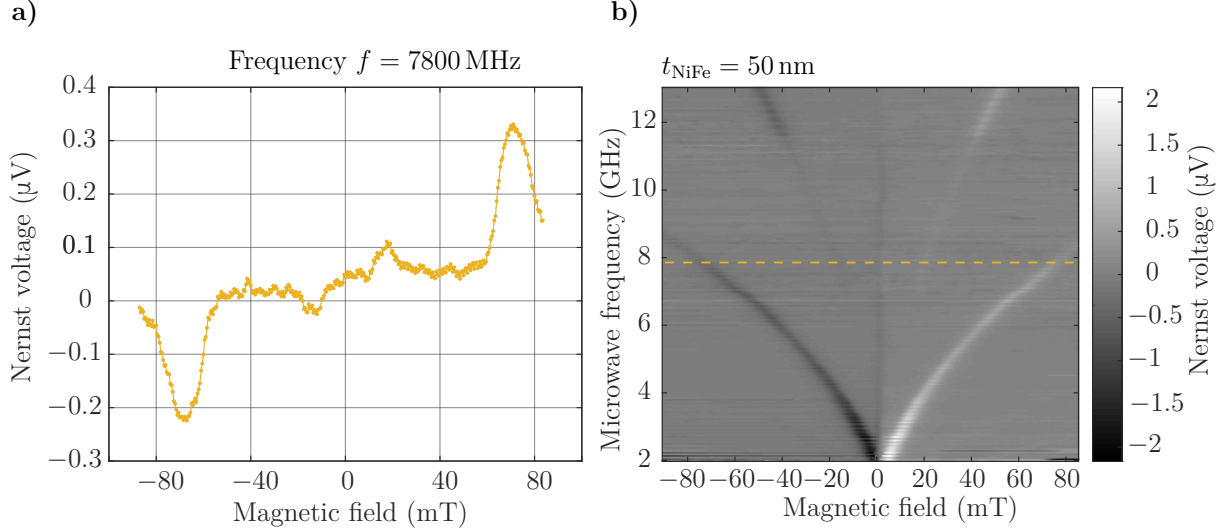
5. RESULTS

a)

b)

Figure 5.1: a) Typical Nernst voltage measurement of the NiFe strip with thickness $t = 100\,\text{nm}$ as a function of the external magnetic field. The width of the NiFe wire was $20\,\mu\text{m}$. The external magnetic field was swept from -90 to $90\,\text{mT}$. The excitation frequency was $f = 7800\,\text{MHz}$. **b)** Grey scale plot for the Nernst voltage corresponding to the spin-wave excitations for different magnetic fields and different excitation frequencies. The thickness of the NiFe strip was $t_{\text{NiFe}} = 50\,\text{nm}$.

In Section 3.3 the experimental setup was described. The most important part of the experiment is the microwave generator Windfreak SynthHD. In the Figure 5.3, the typical harmonic distortion is shown. The essential information is the generation of 2nd and 3rd harmonic frequencies throughout all spectra in the range of $54\,\text{MHz}$ to $13.6\,\text{GHz}$. Very intriguing is the generation of the subharmonic frequencies, when generating fundamental frequencies above $f = 6800\,\text{MHz}$.

The power generated by the microwave generator is in the unit of dBm (*decibel-milliwatt*). The conversion relation between the power in dBm (P_{dBm}) and the power in milliwatts (P_{mW}) is:

$$P_{\text{dBm}} = 10 \cdot \log_{10}\left(\frac{P_{\text{mW}}}{1\,\text{mW}}\right) \tag{5.1}$$

Examples of conversion between dBm and mW can be found in Table 5.1.

Table 5.1: The table shows the relationship between power in dBm or mW and voltage for sinusoidal signals in $50\,\Omega$ systems. The resistivity of the CPW was $R = 33.4\,\Omega$ and current was calculated using Ohm's law. The magnetic field was calculated using FEMM software, see Figure 3.4. The experiment maximum fundamental power $P = 20\,\text{dBm}$ was used.

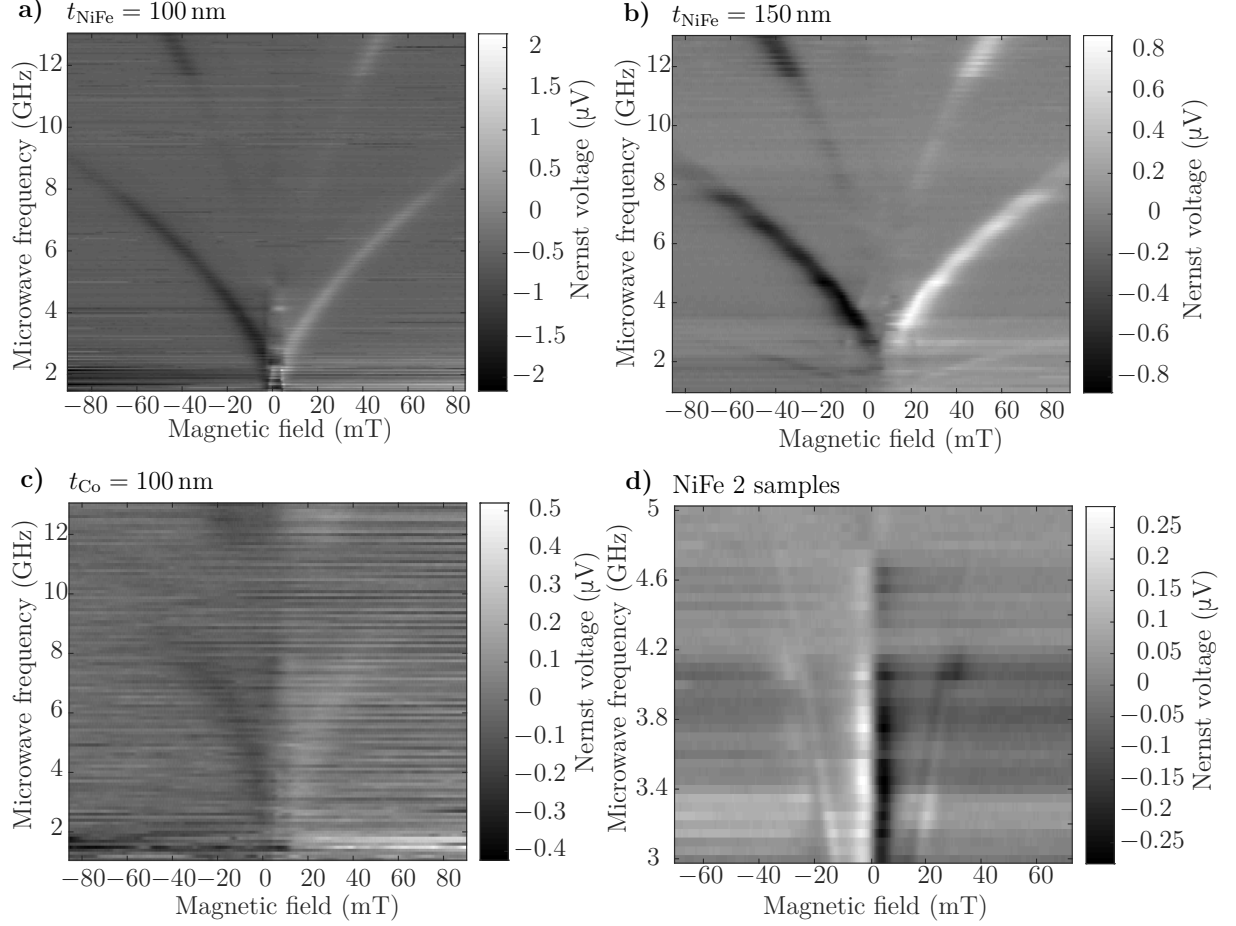| P_{dBm}	-20	-10	0	2	4	5	10	20
P_{mW}	0.01	0.1	1	1.5849	2.5119	3.1628	10	100
U_{mV}	22.361	70.711	223.61	281.51	354.39	397.67	707.11	2236.1
I_{mA}	0.6695	2.1171	6.6948	8.4283	10.611	11.906	21.171	66.948
B_{mT}	0.0353	0.1116	0.353	0.4444	0.5595	0.6278	1.1163	3.53

Figure 5.2: The map of the Nernst voltages generated at the ends of the ferromagnetic wire. The thickness of the NiFe strip was **a)** $t_{NiFe} = 100\,nm$, **b)** $t_{NiFe} = 150\,nm$. **c)** The thickness of the Co strip was $t_{Co} = 100\,nm$. **d)** The NiFe strip with thickness $t = 100\,nm$ was placed on top of the CPW. In this case the frequency was swept from $3\,GHz$ to $5\,GHz$ in $50\,MHz$ steps. This experiment served as a proof of concept, that it is possible to divide the sample prepared by multiple-step lithography into less complicated two samples. Nevertheless, CPW with insulation layer is again prepared by two-step lithography, but in the experimental setup one can use this CPW in combination with various ferromagnetic wires, fabricated by single-step lithography. This might lead to the simpler fabrication of ferromagnetic wires, which may result in faster characterization of magnetodynamic properties of studied materials. The cases **a)**, **b)** and **c)** were fabricated via multi-step lithography process. In contrast, the case **d)** was fabricated using simple lithography process.
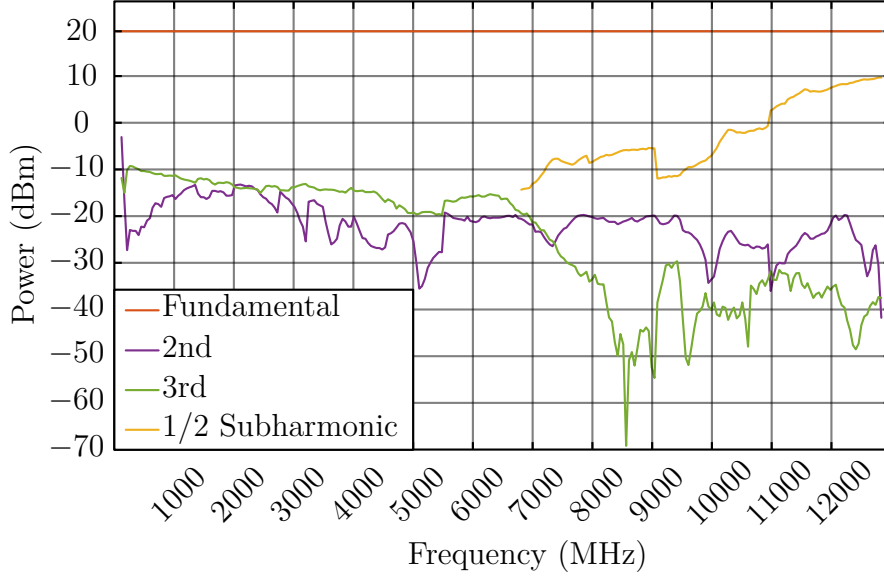
Figure 5.3: The typical Windfreak SynthHD microwave generator harmonic distortion. When generating fundamental frequencies above $f = 6800\,\mathrm{MHz}$, the subharmonic frequencies are created. When using this generator, 2nd and 3rd harmonic frequencies are also created. This data was taken at a maximum fundamental power of $20\,\mathrm{dBm}$. Adapted from [94].

Magnonic crystal

In Section 4.3 the structure with the properties of magnonic crystal was introduced (notched Py strip). In Figure 5.4 the experimentally measured map of the generated Nernst voltages for different external magnetic fields and different microwave excitation frequencies is depicted. The assumption of spectra of spin-wave excitations different than in the case of uniform media was unfortunately not valid for this case. The main cause be-
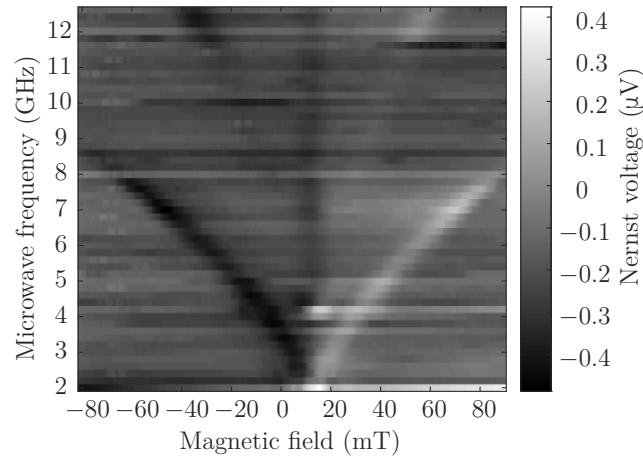
Figure 5.4: Spin-wave spectrum of a magnonic crystal as a function of frequency and external magnetic field.

hind this is the already discussed microwave antenna. Due to the geometry of the antenna (see Section 3.3), only spin waves with $k = 3 \cdot 10^{-3}\,\mathrm{rad/\mu m} \approx 0$ are excited, whereas the wave vector for which the band gap is expected, lies in the order of $k = \pi/a = 6\,\mathrm{rad/\mu m}$. Another possibility might be the detection method itself, since it does not distinguish

between propagating and non-propagating modes, leading to the generation of thermo-electric voltage even when the SWs cannot propagate and are directly attenuated to the lattice (as in the case of rejection band formed by magnonic crystal).

5.2. Analysis

The goal of the measurement was to get magnetodynamic properties of the ferromagnetic materials, such as saturation magnetization M_s, gyromagnetic ratio γ or Gilbert damping α_LLG. In order to get these parameters, the experimental results were analysed. The typical maps are shown in Figure 5.2. To get the saturation magnetization M_s and gyromagnetic ratio γ the peaks, corresponding to the ferromagnetic resonance (FMR), were fitted using Kittel formula:

$$f = \frac{\gamma\mu_0}{2\pi}\left[\left(\frac{B_\mathrm{res}}{\mu_0}\right)\cdot\left(\frac{B_\mathrm{res}}{\mu_0}+M_\mathrm{s}\right)\right]^{1/2},\tag{5.2}$$

where μ_0 is the permeability of free space, B_res is the magnetic resonance field of the FMR mode, γ is the gyromagnetic ratio and M_s is the saturation magnetization.

In Figure 5.5 the map of Nernst voltages generated at the ends of ferromagnetic wire as well as the fits to the Kittel formula (5.2) is shown. The red-branch are the fundamental frequencies set by the control software to microwave generator. The orange-branch are the 1/2 subharmonic parasitic frequencies generated by the microwave generator for the frequencies above 6800 MHz. That means that the orange-branch is actually response of the ferromagnetic material to the subharmonic frequencies, again ferromagnetic resonance. When fitting these results to the Kittel formula (5.2), blue-branch frequency is really double the red-branch frequency.
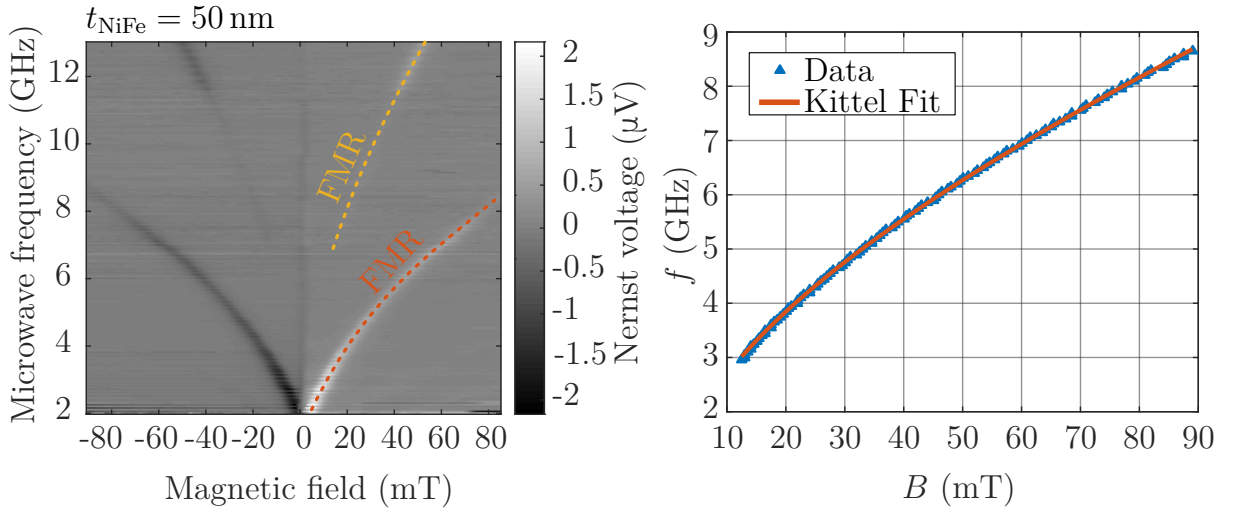

Figure 5.5: Dependence of the excitation frequencies on the resonance field, at which the measured voltages are maximal. The points are in perfect agreement with a fit to the Kittel equation (5.2).

To obtain the Gilbert damping coefficient, α_LLG, see (2.24), the FMR absorption peaks [see Figure 5.6a)] were fitted using Lorentzian fit [95, 96],

$$U = \frac{K_1\Delta B^2 + K_2\Delta B\left(B - B_F\right)}{\Delta B^2 + 4\left(B - B_F\right)^2},\tag{5.3}$$

where K_1 and K_2 are the coefficients of Lorentzian function, B_F is the resonance field of the FMR and ΔB is the linewidth of the FMR, which is determined as the full width at half maximum (FWHM) of the response.
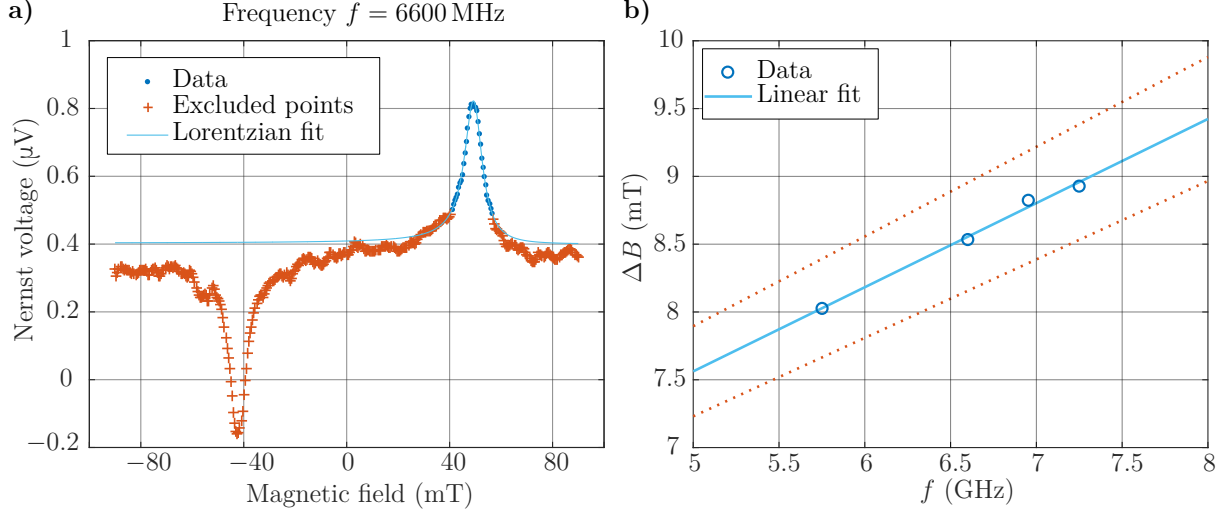

Figure 5.6: a) Fitting of the ferromagnetic resonance (FMR) absorption peaks by Lorentzian fit (5.3). The measured points are blue dots, the points, excluded from fitting are the red crosses and the Lorentzian fit is the blue line. Nernst voltage measurement was done on NiFe film with thickness $t = 100$ nm. The frequency of the excitation microwaves was $f = 6500$ MHz. **b)** The FMR linewidth ΔB as a function of microwave frequency f, obtained from the Lorentzian fit (5.3) of the NiFe film with thickness $t = 100$ nm. The blue solid line is linear fit to (5.4), the red dotted lines are 95% confidence bounds of the linear fit.

The frequency dependent FMR linewidths were then fitted using [97, 98]

$$\Delta B = \Delta B_0 + \frac{4\pi\alpha_{\text{LLG}}}{\gamma}f \,, \tag{5.4}$$

where ΔB_0 is the inhomogeneous broadening, and α_{LLG} is the Gilbert damping coefficient. In Figure 5.6b) the dependence of FMR linewidth on the excitation frequency is shown together with the fit to equation (5.4).

The agreement of the extracted parameters of magnetodynamic properties of NiFe and Co with calculations and other experiments is very good, see Table 5.2.

Table 5.2: Comparison of the extracted parameters (with 95% confidence bounds) of the magnetodynamic properties of NiFe and Co and parameters of magnetodynamic properties from other experiments and calculations.

		$\mu_0 M_{\text{s}}$ (T)	g	$\frac{\gamma}{2\pi}$ (GHz/T)	α_{LLG} (10^{-3})
Experimental data	NiFe	(0.99 ± 0.16)		(27.77 ± 0.28)	(8.6 ± 0.6)
	Co	(1.77 ± 0.04)		(28.8 ± 2.1)	not fitted
Data from references	NiFe	1.04 [16]	2.14 [99]	29.95 [99]	8 [100]
	Co	1.81 [16]	2.18 [101]	30.51 [101]	11 [97]

6. Conclusion

In the presented work, the dynamic phenomena of spin waves in the ferromagnetic strips both with and without properties of magnonic crystals have been investigated by means of anomalous Nernst effect. Therefore, the thesis does not only introduce reader to the young and developing field of research – magnonics, but it also contributes to the deeper understanding of the involved effects and leads to the development of new and efficient ways how to study magnetodynamic properties of ferromagnetic materials.

Within the scope of the thesis, structures were fabricated using single- or multiple-step electron beam lithography (EBL). A cleanness of the sample as well as an accurate alignment were the key parameters to obtain a working sample. As a ferromagnetic material, NiFe or Co were used.

The experimental part of the work has been devoted to the excitation and detection of spin waves. There are several possibilities how to excite and detect spin waves. In the range of thesis, spin waves were locally excited by a dynamic magnetic field generated from a microwave current flowing in a coplanar waveguide (CPW), placed on top of a ferromagnetic strip. The frequencies of the microwave current were in the range of 1 GHz to 13 GHz. The static in-plane magnetic field was applied up to 100 mT. The detection of spin waves in the ferromagnetic wire was done thermoelectrically via anomalous Nernst effect.

Anomalous Nernst effect describes the electric field induced by to formation of temperature gradient generated in the ferromagnetic material due to the relaxation of spin waves to the lattice. The voltage is usually in the µV range and can be measured using common laboratory equipment such as nanovoltmeter. Sweeps of magnetic field for different applied microwave frequencies revealed an electric voltage signature characteristics of spin-wave excitations, with remarkable signal-to-noise ratio.

The magnetodynamic effect, which has been observed, was recognized as a ferromagnetic resonance (FMR) and provides significant understanding of the generation of electromotive forces arising in ferromagnets as a result of magnetization dynamics. The interplay of magnetization dynamics, spin transport, and heat transport is investigated by the emerging field of spin caloritronics.

The ferromagnetic resonance measurements are renowned for the precise determination of the magnetodynamic properties of ferromagnetic materials, such as saturation magnetization M_s, gyromagnetic ratio γ or Gilbert damping α_LLG. FMR are exceptionally appropriate for the characterization of magnetization damping, directly hardly accessible by any other technique. Although magnetization damping has been a subject of many studies, a universal theory of the fundamental contributions is still missing. Therefore, damping remains a phenomenological parameter.

In order to get saturation magnetization M_s and gyromagnetic ratio γ, the dependence of the excitation frequencies on the resonance field, at which the measured voltages are maximal, was fitted using Kittel formula (5.2). Furthermore, the resonance peaks,

were fitted using Lorentzian fit (5.3). The frequency dependent ferromagnetic resonance linewidths were then linearly fitted to obtain the Gilbert damping coefficient α_{LLG}. The extracted parameters, together with the comparison with literature, are listed in Table 5.2.

To summarize, the characterization of magnetodynamic properties of ferromagnetic materials, such as NiFe and Co was successfully done. In future, further optimization of coplanar waveguides (microwave antennas) is needed to obtain even better signal-to-noise ratio and to be able to excite spin waves with appropriate k-vector (in the range of $k = \pi/a$). Additionally, comprehensive study of sensitivity to different spin-wave excitations based on micromagnetic approach should be performed to better understand the magnetodynamic effects in ferromagnetic materials.

References

[1] WOLF, S. A. Spintronics: A Spin-Based Electronics Vision for the Future. *Science.* 2001, vol. 294, no. 5546, 1488–1495. Available from: doi:10.1126/science.1065389.

[2] ŽUTIĆ, I., J. FABIAN and S. D. SARMA. Spintronics: Fundamentals and applications. *Rev. Mod. Phys.* 2004, vol. 76, no. 2, 323–410. Available from: doi:10.1103/RevModPhys.76.323.

[3] BAIBICH, M. N., J. M. BROTO, A. FERT, F. Nguyen VAN DAU, F. PETROFF, P. EITENNE, G. CREUZET, A. FRIEDERICH and J. CHAZELAS. Giant magnetoresistance of (001)Fe/(001)Cr magnetic superlattices. *Phys. Rev. Lett.* 1988, vol. 61, no. 21, 2472–2475. Available from: doi:10.1103/PhysRevLett.61.2472.

[4] BINASCH, G., P. GRÜNBERG, F. SAURENBACH and W. ZINN. Enhanced magnetoresistance in layered magnetic structures with antiferromagnetic interlayer exchange. *Phys. Rev. B.* 1989, vol. 39, no. 7, 4828–4830. Available from: doi:10.1103/PhysRevB.39.4828.

[5] BERGER, L. Emission of spin waves by a magnetic multilayer traversed by a current. *Phys. Rev. B.* 1996, vol. 54, no. 13, 9353–9358. Available from: doi:10.1103/PhysRevB.54.9353.

[6] SLONCZEWSKI, J.C. Current-driven excitation of magnetic multilayers. *J. Magn. Magn. Mater.* 1996, vol. 159, no. 1-2, L1–L7. Available from: doi:10.1016/0304-8853(96)00062-5.

[7] KRUGLYAK, V. V., S. O. DEMOKRITOV and D. GRUNDLER. Magnonics. *J. Phys. D. Appl. Phys.* 2010, vol. 43, no. 26, 264001. Available from: doi:10.1088/0022-3727/43/26/264001.

[8] SERGA, A. A., A. V. CHUMAK and B. HILLEBRANDS. YIG magnonics. *J. Phys. D. Appl. Phys.* 2010, vol. 43, no. 26, 264002. Available from: doi:10.1088/0022-3727/43/26/264002.

[9] KRUGLYAK, V. V. and R. J. HICKEN. Magnonics: Experiment to prove the concept. *J. Magn. Magn. Mater.* 2006, vol. 306, no. 2, 191–194. Available from: doi:10.1016/j.jmmm.2006.02.242.

[10] NIKITOV, S. A., P. TAILHADES and C. S. TSAI. Spin waves in periodic magnetic structures—magnonic crystals. *J. Magn. Magn. Mater.* 2001, vol. 236, no. 3, 320–330. Available from: doi:10.1016/S0304-8853(01)00470-X.

[11] BOONA, S. R., R. C. MYERS and J. P. HEREMANS. Spin caloritronics. *Energy Environ. Sci.* 2014, vol. 7, no. 3, 885–910. Available from: doi:10.1039/c3ee43299h.

[12] BAUER, G. E. W., E. SAITOH and B. J. VAN WEES. Spin caloritronics. *Nat. Mater.* 2012, vol. 11, no. 5, 391–399. Available from: doi:10.1038/nmat3301.

REFERENCES

[13] SCHULTHEISS, H., J. E. PEARSON, S. D. BADER and A. HOFFMANN. Thermoelectric detection of spin waves. *Phys. Rev. Lett.* 2012, vol. 109, no. 23, 237204. Available from: doi:10.1103/PhysRevLett.109.237204.

[14] KITTEL, C. *Introduction to solid state physics.* 8th ed. Hoboken, NJ: Wiley, 2005. ISBN 9780471415268.

[15] BLUNDELL, S. *Magnetism in Condensed Matter.* Oxford: Oxford University Press, 2001. ISBN 9780198505914.

[16] COEY, J. M. D. *Magnetism and Magnetic Materials.* Cambridge: Cambridge University Press, 2010. ISBN 9781139486927.

[17] STÖHR, J. and H. C. SIEGMANN. *Magnetism: From fundamentals to nanoscale dynamics.* Berlin: Springer, 2006. ISBN 978-3-540-30283-4. Available from: doi:10.1007/978-3-540-30283-4.

[18] HILLEBRANDS, B. and K. OUNADJELA. *Spin Dynamics in Confined Magnetic Structures I.* New York: Springer, 2001. ISBN 978-3-540-41191-8. Available from: doi:10.1007/3-540-40907-6.

[19] STANCIL, D. D. and A. PRABHAKAR. *Spin Waves: Theory and Applications.* New York: Springer, 2009. ISBN 978-0-387-77864-8. Available from: doi:10.1007/978-0-387-77865-5.

[20] Van VLECK, J. H. The Theory of Ferromagnetic Resonance. *Phys. Rev.* 1950, vol. 78, no. 3, 266–274. ISSN 0031-899X. Available from: doi:10.1103/PhysRev.78.266.

[21] HUBERT, A. and R. SCHÄFER. *Magnetic Domains: The Analysis of Magnetic Microstructures.* New York: Springer, 2009. ISBN 978-3-540-64108-7. Available from: doi:10.1007/978-3-540-85054-0.

[22] HEISENBERG, W. Zur Theorie des Ferromagnetismus. *Zeitschrift für Phys.* 1928, vol. 49, no. 9-10, 619–636. Available from: doi:10.1007/BF01328601.

[23] CHIKAZUMI, S. *Physics of Ferromagnetism.* 2nd ed. New York: Oxford University Press, 2009. ISBN 0-19-851776-9.

[24] KALINIKOS, B. A. and A. N. SLAVIN. Theory of dipole-exchange spin wave spectrum for ferromagnetic films with mixed exchange boundary conditions. *J. Phys. C Solid State Phys.* 1986, vol. 19, no. 35, 7013–7033. Available from: doi:10.1088/0022-3719/19/35/014.

[25] GUSLIENKO, K. Y., S. O. DEMOKRITOV, B. HILLEBRANDS and A. N. SLAVIN. Effective dipolar boundary conditions for dynamic magnetization in thin magnetic stripes. *Phys. Rev. B.* 2002, vol. 66, no. 13, 132402. Available from: doi:10.1103/PhysRevB.66.132402.

[26] MASON, W. P. Derivation of magnetostriction and anisotropic energies for hexagonal, tetragonal, and orthorhombic crystals. *Phys. Rev.* 1954, vol. 96, no. 2, 302–310. Available from: doi:10.1103/PhysRev.96.302.

[27] DARBY, M. I. and E. D. ISAAC. Magnetocrystalline anisotropy of ferro- and ferrimagnetics. *IEEE Trans. Magn.* 1974, vol. 10, no. 2, 259–304. Available from: doi:10.1109/TMAG.1974.1058331.

[28] LANDAU, L. D. and E. M. LIFSHITZ. On the theory of the Dispersion of Magnetic Permeability in Ferromagnetic Bodies. *Phys. Z. Sowjetunion.* 1935, vol. 8, no. 153, 101–114.

[29] GILBERT, T.L. A phenomenological theory of damping in ferromagnetic materials. *IEEE Trans. Magn.* 2004, vol. 40, no. 6, 3443–3449. Available from: doi:10.1109/TMAG.2004.836740.

[30] BILZER, C. *Microwave susceptibility of thin ferromagnetic films : metrology and insight into magnetization dynamics.* Paris, 2007. PhD thesis. Université Paris Sud - Paris XI.

[31] KRAWCZYK, M. and H. PUSZKARSKI. Plane-wave theory of three-dimensional magnonic crystals. *Phys. Rev. B.* 2008, vol. 77, no. 5, 054437. Available from: doi:10.1103/PhysRevB.77.054437.

[32] HUBER, R. *Control of Spin Waves on the Nanoscale in One-Dimensional Magnonic Crystals and Atomic Layer Deposition of Metallic Ferromagnets for Second Generation of Nanomaterials.* München, 2013. PhD thesis. Technische Universität München.

[33] POLDER, D. On the Quantum Theory of Ferromagnetic Resonance. *Phys. Rev.* 1948, vol. 73, no. 9, 1116–1116. Available from: doi:10.1103/PhysRev.73.1116.

[34] KITTEL, C. On the theory of ferromagnetic resonance absorption. *Phys. Rev.* 1948, vol. 73, no. 2, 155–161. Available from: doi:10.1103/PhysRev.73.155.

[35] BLOCH, F. Zur Theorie des Ferromagnetismus. *Zeitschrift für Phys.* 1930, vol. 61, no. 3, 206–219. Available from: doi:10.1007/BF01339661.

[36] SEBASTIAN, T., K. SCHULTHEISS, B. OBRY, B. HILLEBRANDS and H. SCHULTHEISS. Micro-focused Brillouin light scattering: imaging spin waves at the nanoscale. *Front. Phys.* 2015, vol. 3, 35. Available from: doi:10.3389/fphy.2015.00035.

[37] HERRING, C. and C. KITTEL. On the theory of spin waves in ferromagnetic media. *Phys. Rev.* 1951, vol. 81, no. 5, 869–880. Available from: doi:10.1103/PhysRev.81.869.

[38] DAMON, R. W. and J. R. ESHBACH. Magnetostatic modes of a ferromagnetic slab. *J. Appl. Phys.* 1960, vol. 31, no. 5, S104–S105. Available from: doi:10.1063/1.1984622.

[39] DEMOKRITOV, S. O. and B. HILLEBRANDS. Spinwaves in laterally confined magnetic structures. In: *Spin Dyn. Confin. Magn. Struct. I.* New York: Springer, 2002, 65–93. ISBN 978-3-540-41191-8. Available from: doi:10.1007/3-540-40907-6_3.

[40] KALINIKOS, B.A. Excitation of propagating spin waves in ferromagnetic films. *IEE Proc. H Microwaves, Opt. Antennas.* 1980, vol. 127, no. 1, 4–10. Available from: doi:10.1049/ip-h-1.1980.0002.

[41] ELACHI, C. Magnetic Wave Propagation in a Periodic Medium. *IEEE Trans. Magn.* 1975, vol. 11, no. 1, 36–39. Available from: doi:10.1109/TMAG.1975.1058546.

[42] REED, K. W., J. M. OWENS and R. L. CARTER. Current status of magnetostatic reflective array filters. *Circuits, Syst. Signal Process.* 1985, vol. 4, no. 1-2, 157–180. Available from: doi:10.1007/BF01600078.

REFERENCES

[43] GULYAEV, Y. V., S. A. NIKITOV, L. V. ZHIVOTOVSKII, A. A. KLIMOV, P. TAILHADES, L. PRESMANES, C. BONNINGUE, C. S. TSAI, S. L. VYSOTSKII and Y. A. FILIMONOV. Ferromagnetic films with magnon bandgap periodic structures: Magnon crystals. *J. Exp. Theor. Phys. Lett.* 2003, vol. 77, no. 10, 567–570. Available from: doi:10.1134/1.1595698.

[44] WANG, Z. K., V. L. ZHANG, H. S. LIM, S. C. NG, M. H. KUOK, S. JAIN and A. O. ADEYEYE. Nanostructured magnonic crystals with size-tunable bandgaps. *ACS Nano.* 2010, vol. 4, no. 2, 643–648. Available from: doi:10.1021/nn901171u.

[45] GRUNDLER, D. Reconfigurable magnonics heats up. *Nat. Phys.* 2015, vol. 11, no. 6, 438–441. Available from: doi:10.1038/nphys3349.

[46] CHUMAK, A. V., V. S. TIBERKEVICH, A. D. KARENOWSKA, A. A. SERGA, J. F. GREGG, A. N. SLAVIN and B. HILLEBRANDS. All-linear time reversal by a dynamic artificial crystal. *Nat. Commun.* 2010, vol. 1, 141. Available from: doi:10.1038/ncomms1142.

[47] CHUMAK, A. V., P. PIRRO, A. A. SERGA, M. P. KOSTYLEV, R. L. STAMPS, H. SCHULTHEISS, K. VOGT, S. J. HERMSDOERFER, B. LAEGEL, P. A. BECK and B. HILLEBRANDS. Spin-wave propagation in a microstructured magnonic crystal. *Appl. Phys. Lett.* 2009, vol. 95, no. 26, 262508. Available from: doi:10.1063/1.3279138.

[48] DEMIDOV, V. E., S. O. DEMOKRITOV, B. HILLEBRANDS, M. LAUFENBERG and P. P. FREITAS. Radiation of spin waves by a single micrometer-sized magnetic element. *Appl. Phys. Lett.* 2004, vol. 85, no. 14, 2866–2868. Available from: doi:10.1063/1.1803621.

[49] KHITUN, A., M. BAO and K. L. WANG. Magnonic logic circuits. *J. Phys. D. Appl. Phys.* 2010, vol. 43, no. 26, 264005. Available from: doi:10.1088/0022-3727/43/26/264005.

[50] CSABA, G., A. PAPP and W. POROD. Spin-wave based realization of optical computing primitives. *J. Appl. Phys.* 2014, vol. 115, no. 17, 17C741. Available from: doi:10.1063/1.4868921.

[51] KOSTYLEV, M. P., A. A. SERGA, T. SCHNEIDER, B. LEVEN and B. HILLEBRANDS. Spin-wave logical gates. *Appl. Phys. Lett.* 2005, vol. 87, no. 15, 153501. Available from: doi:10.1063/1.2089147.

[52] SCHNEIDER, T., A. A. SERGA, B. LEVEN, B. HILLEBRANDS, R. L. STAMPS and M. P. KOSTYLEV. Realization of spin-wave logic gates. *Appl. Phys. Lett.* 2008, vol. 92, no. 2, 022505. Available from: doi:10.1063/1.2834714.

[53] LEE, K. S. and S. K. KIM. Conceptual design of spin wave logic gates based on a Mach-Zehnder-type spin wave interferometer for universal logic functions. *J. Appl. Phys.* 2008, vol. 104, no. 5, 053909. Available from: doi:10.1063/1.2975235.

[54] KLINGLER, S., P. PIRRO, T. BRÄCHER, B. LEVEN, B. HILLEBRANDS and A. V. CHUMAK. Design of a spin-wave majority gate employing mode selection. *Appl. Phys. Lett.* 2014, vol. 105, no. 15, 152410. Available from: doi:10.1063/1.4898042.

[55] LÜTH, H. *Solid Surfaces, Interfaces and Thin Films*. Heidelberg: Springer, 2010. 596. ISBN 978-3-642-13591-0. Available from: doi:10.1007/978-3-642-13592-7.

[56] SEEBECK, T. J. Ueber die magnetische Polarisation der Metalle und Erze durch Temperaturdifferenz. *Ann. Phys.* 1826, vol. 82, no. 3, 253–286. Available from: doi:10.1002/andp.18260820202.

[57] PELTIER, J. C. Nouvelles experiences sur la caloricité des courants electrique. *Ann. Chim. Phys.* 1834, vol. 56, no. 371, 371–386.

[58] THOMSON, W. 4. On a Mechanical Theory of Thermo-Electric Currents. *Proceedings of the Royal Society of Edinburgh.* 1857, vol. 3, 91–98. Available from: doi:10.1017/S0370164600027310.

[59] GOLDSMID, H. J. *Introduction to Thermoelectricity.* Heidelberg: Springer, 2010. Springer Series in Materials Science. ISBN 978-3-642-00715-6. Available from: doi:10.1007/978-3-642-00716-3.

[60] HALL, E. H. On a New Action of the Magnet on Electric Currents. *Am. J. Math.* 1879, vol. 2, no. 3, 287–292. Available from: doi:10.1038/021361a0.

[61] HALL, E.H. On the "Rotational Coefficient" in nickel and cobalt. *Philos. Mag. Ser. 5.* 1881, vol. 12, no. 74, 157–172. Available from: doi:10.1080/14786448108627086.

[62] NAGAOSA, N., J SINOVA, S ONODA, A. H. MACDONALD and N. P. ONG. Anomalous Hall effect. *Rev. Mod. Phys.* 2010, vol. 82, no. 2, 1539–1592. Available from: doi:10.1103/RevModPhys.82.1539.

[63] KARPLUS, R. and J. M. LUTTINGER. Hall effect in ferromagnetics. *Phys. Rev.* 1954, vol. 95, no. 5, 1154–1160. Available from: doi:10.1103/PhysRev.95.1154.

[64] PUGH, E. and N. ROSTOKER. Hall Effect in Ferromagnetic Materials. *Rev. Mod. Phys.* 1953, vol. 25, no. 1, 151–157. Available from: doi:10.1103/RevModPhys.25.151.

[65] SMITH, A. W. The variation of the hall effect in metals with change of temperature. *Phys. Rev. (Series I).* 1910, vol. 30, no. 1, 1–34. Available from: doi:10.1103/PhysRevSeriesI.30.1.

[66] UCHIDA, K., S. TAKAHASHI, K. HARII, J. IEDA, W. KOSHIBAE, K. ANDO, S. MAEKAWA and E. SAITOH. Observation of the spin Seebeck effect. *Nature.* 2008, vol. 455, no. 7214, 778–781. Available from: doi:10.1038/nature07321.

[67] CALLEN, H. B. The application of Onsager's reciprocal relations to thermoelectric, thermomagnetic, and galvanomagnetic effects. *Phys. Rev.* 1948, vol. 73, no. 11, 1349–1358. Available from: doi:10.1103/PhysRev.73.1349.

[68] LINDBERG, O. Hall effect. *Proc. IRE.* 1952, vol. 40, no. 11, 1414–1419. Available from: doi:10.1109/JRPROC.1952.273972.

[69] KY, V. D. Planar Hall and Nernst Effect in Ferromagnetic Metals. *Phys. Status Solidi.* 1967, vol. 22, no. 2, 729–736. Available from: doi:10.1002/pssb.19670220242.

[70] MEIER, D., D. REINHARDT, M. SCHMID, C. H. BACK, J. M. SCHMALHORST, T. KUSCHEL and G. REISS. Influence of heat flow directions on Nernst effects in Py/Pt bilayers. *Phys. Rev. B.* 2013, vol. 88, no. 18, 184425. Available from: doi:10.1103/PhysRevB.88.184425.

[71] AVERY, A. D., M. R. PUFALL and B. L. ZINK. Observation of the planar nernst effect in permalloy and Nickel thin films with in-plane thermal gradients. *Phys. Rev. Lett.* 2012, vol. 109, no. 19, 196602. Available from: doi:10.1103/PhysRevLett.109.196602.

REFERENCES

[72] ASHCROFT, N. W. and N. D. MERMIN. *Solid State Physics*. New York: Holt, Rinehart and Winston, 1976. ISBN 978-003-0839-931.

[73] WEILER, M., M. ALTHAMMER, F. D. CZESCHKA, H. HUEBL, M. S. WAGNER, M. OPEL, I. M. IMORT, G. REISS, A. THOMAS, R. GROSS and S. T. B. GOENNENWEIN. Local charge and spin currents in magnetothermal landscapes. *Phys. Rev. Lett.* 2012, vol. 108, no. 10, 106602. Available from: doi:10.1103/PhysRevLett. 108.106602.

[74] KRAUSS, P. R. and S. Y. CHOU. Fabrication of planar quantum magnetic disk structure using electron beam lithography, reactive ion etching, and chemical mechanical polishing. *J. Vac. Sci. Technol. B Microelectron. Nanom. Struct.* 1995, vol. 13, no. 6, 2850–2852. Available from: doi:10.1116/1.588303.

[75] NEW, R. M. H., R. F. W. PEASE and R. L. WHITE. Physical and magnetic properties of submicron lithographically patterned magnetic islands. *J. Vac. Sci. Technol. B Microelectron. Nanom. Struct.* 1995, vol. 13, no. 3, 1089–1094. Available from: doi:10.1116/1.587908.

[76] O'BARR, R., S. Y. YAMAMOTO, S. SCHULTZ, W. XU and A. SCHERER. Fabrication and characterization of nanoscale arrays of nickel columns. *J. Appl. Phys.* 1997, vol. 81, no. 8, 4730–4732. Available from: doi:10.1063/1.365444.

[77] VAŇATKA, M. *Spin vortex states in magnetostatically coupled magnetic nanodisks*. Brno, 2015. Master's thesis. Brno University of Technology. Faculty of Mechanical Engineering. Supervised by Michal URBÁNEK.

[78] RAI-CHOUDHURY, P. *Handbook of Microlithography, Micromachining, and Microfabrication: Microlithography*. London: SPIE Press, 1997. ISBN 9780819423788.

[79] ZHOU, W. and Z. L. WANG. *Scanning microscopy for nanotechnology: Techniques and applications*. New York: Springer, 2007. 522. ISBN 978-0-387-33325-0. Available from: doi:10.1007/978-0-387-39620-0.

[80] BABOCKÝ, J. *Optical Response of Asymmetric Plasmonic Structures*. Brno, 2014. Master's thesis. Brno University of Technology. Faculty of Mechanical Engineering. Supervised by Jan ČECHAL.

[81] WASA, K, I. KANNO and K. HIDETOSHI. *Handbook of Sputter Deposition Technology Fundamentals and Applications for Functional Thin Films, Nanomaterials, and MEMS*. 2nd ed. Waltham, MA: William Andrew, 2012. ISBN 0815512805. Available from: doi:10.1016/B978-1-4377-3483-6.00006-1.

[82] HARSHA, K. S. S. *Principles of Physical Vapor Deposition of Thin Films*. Burlington: Elsevier, 2006. ISBN 9780080480312.

[83] SEBASTIAN, T., Y. OHDAIRA, T. KUBOTA, P. PIRRO, T. BRÄCHER, K. VOGT, A. A. SERGA, H. NAGANUMA, M. OOGANE, Y. ANDO and B. HILLEBRANDS. Low-damping spin-wave propagation in a micro-structured $Co_2Mn_{0.6}Fe_{0.4}Si$ Heusler waveguide. *Appl. Phys. Lett.* 2012, vol. 100, no. 11, 112402. Available from: doi:10.1063/1.3693391.

[84] KIRILYUK, A., A. V. KIMEL and T. RASING. Ultrafast optical manipulation of magnetic order. *Rev. Mod. Phys.* 2010, vol. 82, no. 3, 2731–2784. Available from: doi:10.1103/RevModPhys.82.2731.

[85] SATOH, T., Y. TERUI, R. MORIYA, B. A. IVANOV, K. ANDO, E. SAITOH, T. SHIMURA and K. KURODA. Directional control of spin-wave emission by spatially shaped light. *Nat. Photonics.* 2012, vol. 6, no. 10, 662–666. Available from: doi:10.1038/nphoton.2012.218.

[86] NEUSSER, S. *Spin Waves in Antidot Lattices : From Quantization to Magnonic Crystals.* München, 2011. PhD thesis. Technische Universität München.

[87] NEUSSER, S., G. DUERR, H. G. BAUER, S. TACCHI, M. MADAMI, G. WOLTERSDORF, G. GUBBIOTTI, C. H. BACK and D. GRUNDLER. Anisotropic propagation and damping of spin waves in a nanopatterned antidot lattice. *Phys. Rev. Lett.* 2010, vol. 105, no. 6, 067208. Available from: doi:10.1103/PhysRevLett.105.067208.

[88] WEN, C.P. Coplanar Waveguide: A Surface Strip Transmission Line Suitable for Nonreciprocal Gyromagnetic Device Applications. *IEEE Trans. Microw. Theory Tech.* 1969, vol. 17, no. 12, 1087–1090. Available from: doi:10.1109/TMTT.1969.1127105.

[89] SIMONS, Rainee N. *Coplanar waveguide circuits, components, and systems.* Hoboken, NJ: John Wiley & Sons, 2004. Available from: doi:10.1002/0471224758.

[90] VLAMINCK, V. and M. BAILLEUL. Spin-wave transduction at the submicrometer scale: Experiment and modeling. *Phys. Rev. B.* 2010, vol. 81, no. 1, 014425. Available from: doi:10.1103/PhysRevB.81.014425.

[91] SEKIGUCHI, K., K. YAMADA, S. M. SEO, K. J. LEE, D. CHIBA, K. KOBAYASHI and T. ONO. Time-domain measurement of current-induced spin wave dynamics. *Phys. Rev. Lett.* 2012, vol. 108, no. 1, 017203. Available from: doi:10.1103/PhysRevLett.108.017203.

[92] PIRRO, P., T. BRÄCHER, K. VOGT, B. OBRY, H. SCHULTHEISS, B. LEVEN and B. HILLEBRANDS. Interference of coherent spin waves in micron-sized ferromagnetic waveguides. *Phys. Status Solidi.* 2011, vol. 248, no. 10, 2404–2408. Available from: doi:10.1002/pssb.201147093.

[93] VOGT, K., H. SCHULTHEISS, S. J. HERMSDOERFER, P. PIRRO, A. A. SERGA and B. HILLEBRANDS. All-optical detection of phase fronts of propagating spin waves in a Ni81 Fe19 microstripe. *Appl. Phys. Lett.* 2009, vol. 95, no. 18, 182508. Available from: doi:10.1063/1.3262348.

[94] GOINS, David. *Windfreak Technologies, SynthHD: 54 MHz–13.6 GHz Dual Channel Microwave Signal Generator* [online]. 2016 [Accesed 2017-05-09]. Available from: https://windfreaktech.com/wp-content/uploads/docs/synthhd/SynthHD-dual-channel-microwave-signal-generator.pdf.

[95] KALARICKAL, S. S., P. KRIVOSIK, M. WU, C. E. PATTON, M. L. SCHNEIDER, P. KABOS, T. J. SILVA and J. P. NIBARGER. Ferromagnetic resonance linewidth in metallic thin films: Comparison of measurement methods. *J. Appl. Phys.* 2006, vol. 99, no. 9, 093909. Available from: doi:10.1063/1.2197087.

[96] YIN, Y., F. PAN, M. AHLBERG, M. RANJBAR, P. DURRENFELD, A. HOUSHANG, M. HAIDAR, L. BERGQVIST, Y. ZHAI, R. K. DUMAS, A. DELIN and J. AKERMAN. Tunable permalloy-based films for magnonic devices. *Phys. Rev. B.* 2015, vol. 92, no. 2, 024427. Available from: doi:10.1103/PhysRevB.92.024427.

REFERENCES

[97] WOLTERSDORF, G. *Spin-pumping and two-magnon scattering in magnetic multi-layers*. Vancouver, 2004. PhD thesis. Simon Fraser University.

[98] WOLTERSDORF, G., M. KIESSLING, G. MEYER, J-U. THIELE and CH. BACK. Damping by slow relaxing rare earth impurities in $Ni_{80}Fe_{20}$. *Phys. Rev. Lett.* 2009, vol. 102, no. 25, 257602. Available from: doi:10.1103/PhysRevLett.102.257602.

[99] GUBBIOTTI, G., O. KAZAKOVA, G. CARLOTTI, M. HANSON and P. VAVAS-SORI. Spin-Wave Spectra in Nanometric Elliptical Dots Arrays. *IEEE Trans. Magn.* 2003, vol. 39, no. 5, 2750–2752. Available from: doi:10.1109/TMAG.2003.815588.

[100] GERRITS, T., J. HOHLFELD, O. GIELKENS, K. J. VEENSTRA, K. BAL, T. RASING and H. A M. VAN DEN BERG. Magnetization dynamics in NiFe thin films induced by short in-plane magnetic field pulses. *J. Appl. Phys.* 2001, vol. 89, no. 11, 7648–7650. Available from: doi:10.1063/1.1359462.

[101] PELZL, J., R. MECKENSTOCK, D. SPODDIG, F. SCHREIBER, J. PFLAUM and Z. FRAIT. Spin–orbit-coupling effects on g-value and damping factor of the ferromagnetic resonance in Co and Fe films. *J. Phys. Condens. Matter.* 2003, vol. 15, no. 5, S451–S463. Available from: doi:10.1088/0953-8984/15/5/302.

List of abbreviations

AESWS   all electrical spin-wave spectroscopy

AHE   anomalous Hall effect

ANE   anomalous Nernst effect

BLS   Brillouin light scattering

CEITEC   Central European Institute of Technology

CMOS   complementary metal-oxide-semiconductor

CPW   coplanar waveguide

EBL   electron beam lithography

FEMM   finite element method magnetics

FFT   fast Fourier transformation

FMR   ferromagnetic resonance

FWHM   full width at half maximum

GMR   giant magnetoresistance

GPIB   general purpose interface bus

IC   inner conductor

IPA   isopropyl alcohol

IPE BUT   Institute of Physical Engineering, Brno University of Technology

LIS   laser interferometer stage

LL   Landau-Lifschitz equation

LLG   Landau-Lifschitz-Gilbert equation

MOKE   magneto optical Kerr effect

MSBVW   magnetostatic backward volume waves

MSFVW   magnetostatic forward volume waves

LIST OF ABBREVIATIONS

MSSW	magnetostatic surface waves
OC	outer conductor
PCB	printed circuit board
PGMEA	propylene glycol monomethyl ether acetate
PMMA	Poly(methyl methacrylate) (positive e-beam resist)
PSSW	perpendicular standing spin waves
Py	permalloy
SEM	scanning electron microscope
SMA	subminiature version A
SSE	spin Seebeck effect
STT	spin transfer torque
SW	spin waves
TMAH	tetramethylammonium hydroxide
UHV	ultrahigh vacuum
USB	universal serial bus
VNA-FMR	vector network analyzer ferromagnetic resonance

Symbols and constants

A_{ex}	exchange stiffness [J·m^{-1}]
$\boldsymbol{B}$	B-field, magnetic flux density [T]
d	distance [m]
D_{ij}	dipole-dipole interaction strength [T·A^{-1}·m^{-2}]
$\boldsymbol{E}$	electric field [V·m^{-1}]
f	frequency [Hz]
$\boldsymbol{F}$	force [N]
g	Landé g-factor
h	harmonic magnetic field [A·m^{-1}]
$\boldsymbol{H}$	H-field, magnetic field strength [A·m^{-1}]
$\mathcal{H}$	quantum mechanical Hamiltonian of ferromagnetism
$\boldsymbol{H}_{\text{dem}}$	demagnetizing magnetic field [A·m^{-1}]
$\boldsymbol{H}_{\text{eff}}$	effective magnetic field [A·m^{-1}]
$\boldsymbol{H}_{\text{ext}}$	external magnetic field [A·m^{-1}]
$\mathcal{H}_{\text{ex}}$	exchange interaction Hamiltonian
i	longitudinal electric current density [A·m^{-1}]
i	imaginary unit, $\text{i} = \sqrt{-1}$
I	electric current [A]
j	electric current density [A·m^{-2}]
J	exchange constant
$\boldsymbol{k}$	wave vector [rad·m^{-1}]
$\boldsymbol{k}_p$	out-of-plane component of wave vector [rad·m^{-1}]
$\boldsymbol{k}_\zeta$	in-plane component of wave vector [rad·m^{-1}]

SYMBOLS AND CONSTANTS

$k_\parallel$	in-plane component of wave vector, parallel to the magnetic field [rad·m^{-1}]
$k_\perp$	in-plane component of wave vector, perpendicular to the magnetic field [rad·m^{-1}]
K_1, K_2	coefficient of Lorentzian functions
K_u	anisotropy constant [J·m^{-3}]
$\boldsymbol{L}$	angular momentum [V·A·s^2]
$\boldsymbol{m}$	dynamic component of the magnetization [A·m^{-1}]
$\boldsymbol{M}$	magnetization [A·m^{-1}]
M_s	saturation magnetization [A·m^{-1}]
N	demagnetizing field factor
N	Nernst coefficient [V·T^{-1}·K^{-1}]
N_A	anomalous Nernst coefficient [V·T^{-1}·K^{-1}]
p	imaginary magnetic charge
P	Ettingshausen coefficient [K·A^{-1}·T^{-1}]
P	Power [W]
$\boldsymbol{r}_{ij}$	vector between spin i and j [m]
R	Righi–Leduc coefficient [T^{-1}]
R_a	anomalous Hall coefficient [Ω·T^{-1}]
R_o	ordinary Hall coefficient [Ω·T^{-1}]
s_icoc	distance between the centre conductor and outer conductor edges [m]
$\boldsymbol{S}$	spin angular momentum [kg·m^2·s^{-1}]
S	Seebeck coefficient [V·K^{-1}]
t	time [s]
t	thickness [m]
$\boldsymbol{T}$	torque [N·m]
T	temperature [K]
$\boldsymbol{v}$	velocity [m·s^{-1}]
v_g	group velocity [m·s^{-1}]
v_{ph}	phase velocity [m·s^{-1}]
V	volume [m^3]

w_{ic}	width of inner conductor [m]
w_{oc}	width of outer conductor [m]
α_{LLG}	Gilbert damping parameter
γ	gyromagnetic ratio [C·kg^{-1}]
ϵ_{dem}	demagnetizing field energy density [J·m^{-3}]
ϵ_{ex}	exchange energy density [J·m^{-3}]
ϵ_{tot}	total energy density [J·m^{-3}]
ϵ_{uni}	energy density of an uniaxial anisotropy [J·m^{-3}]
ϵ_Z	Zeeman energy density [J·m^{-3}]
λ	thermal conductivity [W·m^{-1}·K^{-1}]
λ	Landau damping parameter
λ	wavelength [m]
$\boldsymbol{\mu}$	magnetic moment [A·m^2]
μ_B	Bohr magneton ($\mu_B = 9.274 \cdot 10^{-24}$ J·T^{-1})
μ_0	magnetic permeability of free space ($\mu_0 = 4\pi \cdot 10^{-7}$ H·m^{-1})
Π	Peltier coefficient [V]
ϱ_H	Hall resistivity [Ω]
ϱ_M	magnetic charge density [A·m^{-2}]
ϕ	magnetic scalar potential [A]
χ	susceptibility of material
ω	angular frequency [rad·s^1]

---

[*]The values were selected from the 2014 CODATA recommended values www.physics.nist.gov.

A. Appendices

A.1. Landau-Lifshitz-Gilbert equation

To prove the equivalence of (2.24) and (2.25) we start from (2.25) and insert for the last term the entire expression of $\frac{\partial \boldsymbol{M}}{\partial t}$ to obtain

$$\frac{\partial \boldsymbol{M}}{\partial t} = -\gamma \left[\boldsymbol{M} \times \boldsymbol{H}\right] + \frac{\alpha_{\text{LLG}}}{M_{\text{s}}} \left[\boldsymbol{M} \times \left(-\gamma \left[\boldsymbol{M} \times \boldsymbol{H}\right] + \frac{\alpha_{\text{LLG}}}{M_{\text{s}}} \left[\boldsymbol{M} \times \frac{\partial \boldsymbol{M}}{\partial t}\right]\right)\right] , \qquad (A.1)$$

$$\frac{\partial \boldsymbol{M}}{\partial t} = -\gamma \left[\boldsymbol{M} \times \boldsymbol{H}\right] - \frac{\gamma \alpha_{\text{LLG}}}{M_{\text{s}}} \left[\boldsymbol{M} \times \left(\boldsymbol{M} \times \boldsymbol{H}\right)\right] + \frac{\alpha_{\text{LLG}}^2}{M_{\text{s}}^2} \left[\boldsymbol{M} \times \left(\boldsymbol{M} \times \frac{\partial \boldsymbol{M}}{\partial t}\right)\right] . \qquad (A.2)$$

By the use of cross product rule

$$\boldsymbol{a} \times \left(\boldsymbol{b} \times \boldsymbol{c}\right) = \boldsymbol{b} \left(\boldsymbol{a} \cdot \boldsymbol{c}\right) - \boldsymbol{c} \left(\boldsymbol{a} \cdot \boldsymbol{b}\right) \qquad (A.3)$$

we get

$$\boldsymbol{M} \times \left(\boldsymbol{M} \times \frac{\partial \boldsymbol{M}}{\partial t}\right) = \boldsymbol{M} \underbrace{\left(\boldsymbol{M} \cdot \frac{\partial \boldsymbol{M}}{\partial t}\right)}_{0} - \frac{\partial \boldsymbol{M}}{\partial t} \underbrace{\left(\boldsymbol{M} \cdot \boldsymbol{M}\right)}_{M_{\text{s}}^2} . \qquad (A.4)$$

$\boldsymbol{M}$ and $\frac{\partial \boldsymbol{M}}{\partial t}$ are perpendicular so the scalar product is zero. Magnetization $\boldsymbol{M}$ is by definition the magnetic moment $\boldsymbol{\mu}$ of a sample per volume V. The magnetic moments are conserved, therefore $|\boldsymbol{M}(\boldsymbol{r})| = M_{\text{s}}$, the saturation magnetization, stays constant. We derive the result

$$\frac{\partial \boldsymbol{M}}{\partial t} = -\gamma \left[\boldsymbol{M} \times \boldsymbol{H}\right] - \frac{\gamma \alpha_{\text{LLG}}}{M_{\text{s}}} \left[\boldsymbol{M} \times \left(\boldsymbol{M} \times \boldsymbol{H}\right)\right] - \alpha_{\text{LLG}}^2 \frac{\partial \boldsymbol{M}}{\partial t} , \qquad (A.5)$$

which is the same as (2.24).